Inactivation of Influenza A virus by pH conditions encountered in expiratory aerosol particles results from localized conformational changes within Haemagglutinin and Matrix 1 proteins.

Shannon C. David[1], Oscar Vadas[2#], Irina Glas[3#], Aline Schaub[1], Beiping Luo[4], Giovanni D'Angelo[5], Jonathan Paz Montoya[5], Nir Bluvshtein[4], Walter Hugentobler[6], Liviana K. Klein[4], Ghislain Motos[6], Marie Pohl[3], Kalliopi Violaki[6], Athanasios Nenes[6,7], Ulrich K. Krieger[4], Silke Stertz[3], Thomas Peter[4], and Tamar Kohn[1]*.

[1]Environmental Chemistry Laboratory, School of Architecture, Civil and Environmental Engineering, Ecole Polytechnique Federale de Lausanne (EPFL), Lausanne, Switzerland

[2]Protein Platform, Faculty of Medicine, University of Geneva, Geneva, Switzerland

[3]Institute of Medical Virology, University of Zurich, Zürich, Switzerland

[4]Institute for Atmospheric and Climate Science, ETH Zurich, Zurich, Switzerland

[5]Laboratory of Lipid Cell Biology, Interschool Institute of Bioengineering and Global Health Institute, School of Life Sciences, Ecole Polytechnique Federale de Lausanne (EPFL), Lausanne, Switzerland

[6]Laboratory of Atmospheric Processes and their Impacts, School of Architecture, Civil and Environmental Engineering, Ecole Polytechnique Federale de Lausanne (EPFL), Lausanne, Switzerland

[7]Institute of Chemical Engineering Sciences, Foundation for Research and Technology Hellas, Patras, Greece

[#]Equal contribution

*Corresponding author: tamar.kohn@epfl.ch

ABSTRACT

Multiple respiratory viruses including Influenza A virus (IAV) can be transmitted via expiratory aerosol particles, and many studies have established that indoor environmental conditions can affect viral infectivity during this transmission. Aerosol pH was recently identified as a major factor influencing the infectivity of aerosol-borne IAV and SARS-CoV-2, and for indoor room air, modelling indicates that small exhaled aerosols will undergo rapid acidification (pH below 5.5). However, there is a fundamental lack of understanding as to the mechanisms leading to viral inactivation within an acidic aerosol micro-environment. Here, we identified that transient exposure to acidic conditions impacted the early stages of the IAV infection cycle, which was primarily attributed to loss of binding function of the viral protein haemagglutinin. Viral capsid integrity was also partially affected by transient acidic exposures. The structural changes associated with loss of viral infectivity were then characterized using whole-virus hydrogen-deuterium exchange coupled to mass spectrometry (HDX-MS), and we observed discrete regions of unfolding in the external viral protein haemagglutinin and the internal matrix protein 1. Viral nucleoprotein structure appeared to be unaffected by exposure to acidic conditions. Protein analyses were complemented by genome and lipid envelope characterizations, and no acid-mediated changes were detected using our whole-virus methods. Improved understanding of the fate of respiratory viruses within exhaled aerosols constitutes a global public health priority, and information gained here could aid the development of novel strategies or therapeutics to control the airborne persistence of seasonal and/or pandemic influenza in the future. This study also provides proof-of-concept that HDX-MS is a highly effective method for characterization of both internal and external proteins for whole enveloped viruses such as IAV.

INTRODUCTION

Airborne transmission of infectious agents relies on the ability of pathogens to survive aerosol transport whilst they transit between hosts. Evidence in the literature increasingly points towards the expiratory aerosol as a key transmission mode for many respiratory viruses, including SARS-CoV-2 (1–7), human rhinovirus (8–11), respiratory syncytial virus (12), human adenovirus (13), and influenza A virus (IAV) (14–23). This route also dominates under certain environmental conditions, particularly indoor environments that are poorly ventilated. In one study, airborne transmission was estimated to account for half of all transmission events of IAV in households (19). Human volunteer studies have also suggested that inhalation of aerosolized IAV results in a lower dose required to establish infection, and causes more severe symptoms when compared to intranasal inoculation (which mimics contact or droplet transmission) (24,25). Identifying factors that can drive inactivation of airborne pathogens within these indoor aerosols will be critical to mitigate infection risks and control new respiratory outbreaks in the future.

However, there continues to be a fundamental lack of understanding as to what determines viral fate within expiratory aerosols. Upon exhalation, aerosols will rapidly lose both moisture and heat, with a large concomitant change in volume as they establish an equilibrium with the indoor environment. Numerous studies have attempted to assess how this drying process affects viral infectivity, with infectivity being lost or maintained depending on the selected conditions and the virus of interest. Many individual factors are postulated to influence viral infectivity (e.g. temperature, salt concentration, relative humidity, presence of respiratory proteins or surfactants, and air/liquid interface interactions (26–29)), though few studies have decoupled single factors from the others to allow for mechanistic characterizations. Aerosol pH is a particular factor that has previously been overlooked, with recent studies showing a pronounced effect of aerosol pH on infectivity for IAV and SARS-CoV-2 (30,31). Depending on the particle size, the pH of expelled droplets and smaller exhaled aerosols quickly deviates from neutral. For particles expelled into normal room air, the internal pH is proposed to initially increase prior to acidification (30–32). For small aerosol particles in particular, this acidification is thought to occur almost immediately after exhalation (30,32). Given that respiratory viruses are reported to be enriched within smaller aerosol particles ≤5 μm (23,33–37), we sought to investigate the effect of this acidic aerosol pH on the structural integrity and infectivity of IAV.

IAV presents certain challenges for structural analysis as it is a complex virion comprised of at least 11 individual proteins, some of which are membrane embedded or associated, and the surface-exposed proteins are also highly glycosylated. Glycoproteins have proved to be challenging for structural biology due to the intrinsic flexibility and heterogeneity of the glycan decorations (38). To gain high-resolution information on potential changes occurring to IAV proteins under acidic aerosol conditions, we utilized hydrogen-deuterium exchange coupled to mass-spectrometry (HDX-MS). This

structural method can assess local as well as global conformational changes of proteins in their near-native environment. HDX-MS exploits a fundamental property of protein amide hydrogens, whose rate of exchange is dependent on the structural environment of individual amides. Those forming stable hydrogen bonds, as in α-helices or β-sheet secondary structures, will exchange several orders of magnitude more slowly than exposed amides (39). By incubating a protein of interest in deuterated buffer (D_2O), amide hydrogens will passively exchange for deuterium. Changes in the local structure of a given protein segment can therefore be distinguished by comparing amide exchanges rates of peptic peptides of the same protein exposed to different conditions (38). Whilst HDX-MS has been primarily used to study soluble proteins, it has become possible to also analyze the structure of membrane-bound proteins (40,41) and proteins contained within whole virus capsids (42–47). Two studies have applied HDX-MS to study whole IAV in the past, with both focusing on the effect of host endosomal pH (~5.5) on the glycoprotein haemagglutinin (HA) (48,49). To expand these initial studies, we analyzed whole-virus samples for low pH-induced structural changes to surface-bound HA, as well as changes to internal viral proteins matrix 1 (M1) and nucleoprotein (NP). To decouple the effect of pH from other factors present within the evaporating aerosol micro-environment, we performed this study in bulk solutions with controlled pH values. Importantly, the pH of interest for this study is far below that of the fusion pH investigated previously. All experiments were performed at ambient temperatures to mimic typical indoor air conditions. To complement the study on protein structure and obtain a global analysis of the state of IAV, integrity of the viral genome and viral lipids were also assessed under acidic aerosol conditions.

RESULTS

IAV is rapidly inactivated under expiratory aerosol conditions.

The majority of exhaled aerosols from humans are <5 µm, with a large fraction being <1 µm for most respiratory activities (8,50). Previous studies have specifically identified influenza virus in aerosols of these sizes, generated by coughing and normal breathing by infected individuals (36,51,23). Upon exhalation, these aerosols rapidly lose water and equilibrate with acidic and basic trace gases present in room air, including nitric acid and ammonia. We have previously used a biophysical Respiratory Aerosol Model (ResAM) to show an exhaled particle of 1 µm initial radius will acidify to a pH ~4 due to this equilibration (30). Depending on the initial size of the particle, the pH development will vary. Here, ResAM was used to estimate the pH trajectory of exhaled particles of 3 different initial sizes (0.2 µm, 1 µm, and 5 µm radius), representative of the range of 'fine' aerosols produced by humans. ResAM predicted that the same terminal acidic pH of ~4 would be reached for all 3 particle sizes, with the smallest modelled particle size reaching this point less than 10 seconds post-exhalation (**Fig. 1A**). With larger particles, more time is needed for the diffusion of trace acids into the particle, thus the acidification process was predicted to be slower by ResAM, though a terminal pH of 4 was reached in all cases.

IAV is known to be highly sensitive to acidic pH, thus we sought to determine mechanisms by which this acidic aerosol environment could affect IAV structural integrity and impair discrete stages of the IAV infectious cycle. To eliminate the effect of varying acidification times resulting from differing aerosol sizes, these experiments were performed in bulk pH-adjusted salt solutions (see Methods for compositions). Initially, IAV was spiked into acidic (pH 4) or neutral (pH 7) conditions, then aliquots were taken and neutralized at varying time-points for quantification of remaining infectious titers. Infectivity data (**Fig. 1B**) show that exposure to pH 4 at room temperature results in rapid virus inactivation, with infectious viral titers decaying by approximately 3-$\log_{10}$ within 10 seconds of pH 4 exposure, and by >5-$\log_{10}$ by 30 seconds. Conversely, IAV spiked into pH 7 solution or PBS (both neutral controls) and held at the same ambient temperature showed minimal decay for the full 24-hour monitoring period. These kinetics are similar to those previously observed, and it has been established that aggregation of whole viral particles in acidic conditions does not skew infectivity results in our system (30).

In order to reveal the pH-induced changes to the virus responsible for this infectivity loss, we monitored potential accumulation of viral NP within host cells at early time points post-infection. Virus samples exposed to pH 4 for 10 and 30 seconds prior to neutralization showed no productive infection in host cells at either 3 hours (**Fig. 1C**) or 6 hours post-infection (**Supplementary Fig. S1**) when compared to neutral controls, indicating that an early step of the infection cycle was specifically targeted by low pH treatment. We hypothesized that the observed loss of productive infection was

due to a conformational change in viral protein HA, which usually occurs between pH 5.5–5 in host-cell endosomes. This change allows HA to mediate membrane fusion between the endosome and the viral envelope, and allows viral uncoating and entry to proceed. The 'pH-activated' form of HA is often referred to as the post-fusion conformation. However, the 'pre-fusion' form of HA is critical for host cell attachment by binding to sialic acid receptors, and if the post-fusion conformation is attained prematurely (e.g. via acidic exposure within an aerosol), HA will be unable to bind host cells.

To confirm whether the viral decay was indeed mediated by HA structural rearrangement, pseudotyped Vesicular stomatitis virus (VSV) strains were used. VSV was pseudotyped with IAV surface proteins HA and neuraminidase (NA), generating VSV-H1N1, which was pH exposed in bulk solution and neutralized in the same manner as wild-type IAV. Inactivation kinetics of the pseudotyped VSV strain at pH 4 were very similar to inactivation of wild-type IAV, with ~3-$\log_{10}$ decrease in infectivity after 10 seconds pH-exposure, and residual infectivity being below detection limits by 30 seconds (**Fig. 1D**). Control VSV expressing wild-type G protein showed no loss of infectivity as a result of the same pH treatment and neutralization. Importantly, VSV G protein undergoes a similar low pH conformational change like IAV HA to mediate envelope fusion with host cells, but the change to G protein is entirely reversible (52). As IAV NA also does not function in viral attachment or uncoating inside host cells, this indicates that the majority of virus inactivation observed under acidic conditions for pseudotyped VSV was mediated by non-reversible changes to HA. In support of this, fluorescence imaging of whole pH-treated IAV particles showed increased staining for the post-fusion form of HA (detected with monoclonal antibody Y8-10C2, validated in (53) to bind more strongly to post-fusion HA) after 10 seconds of pH 4 exposure (**Fig. 1E**), whilst the post-fusion form of HA was minimally present on pH 7-treated viruses. Some low-level signal was observed at pH 7, however this was attributed to background staining. Staining for internal nucleoprotein (NP) ensured the same amount of viral material was imaged in all cases.

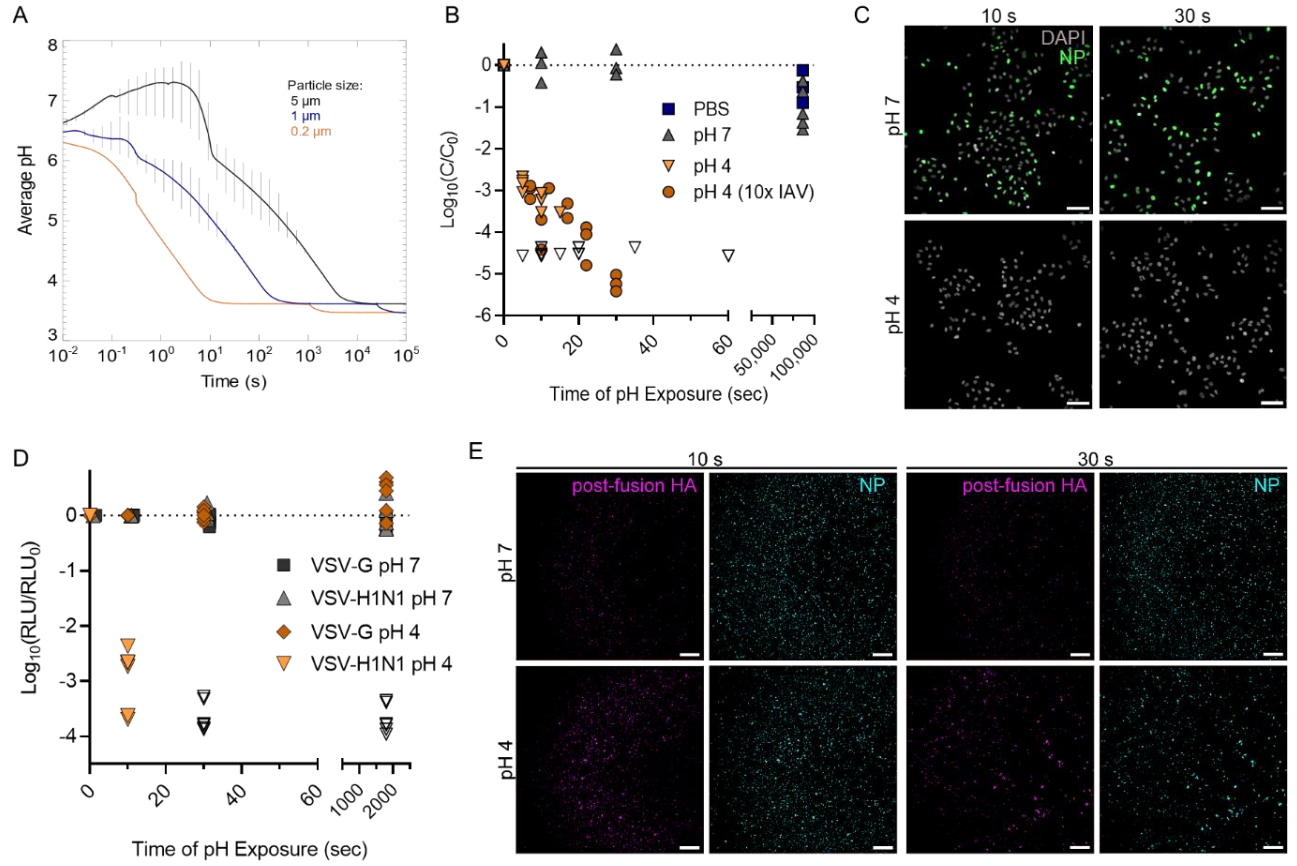

Figure 1 – Acidification of an exhaled aerosol, and the effect on IAV infectivity. A) Average pH within an exhaled respiratory aerosol particle as it transitions from the nasal microenvironment to typical indoor air, modelled using ResAM. The particle evaporates with time (in seconds), resulting in acidification down to ~pH 3.8. Progressive changes in pH are modelled for particles of 3 different initial sizes. Vertical error bars indicate the pH range between the innermost and outermost aerosol shells at each timepoint, with the mean pH presented as a continuous line. Thermodynamic and kinetic properties are those of synthetic lung fluid (SLF), a representative respiratory matrix. The indoor air conditions were set at 20°C and 50% RH, and the exhaled air is assumed to mix into the indoor air using a turbulent eddy diffusion coefficient of 50 cm^2 /s. **B)** Inactivation of IAV due to exposure to acidic pH 4. IAV was spiked into neutral solutions of PBS or pH 7 buffer, or spiked into acidic pH 4 buffer. Aliquots were taken at multiple time-points post spiking (up to 86,400 sec, or 24 hours), and neutralized for quantification of remaining viral titer by plaque assay. For pH 4 samples, virus was spiked at 10^6 PFU/mL, or at 10^7 PFU/mL (10x IAV), to demonstrate that viral concentration did not affect the rate of viral decay. Data points indicate the mean ± SD of triplicate measurements at each time-point, presented as $\log_{10}$ of remaining concentration (C) at each time-point relative to the initial concentration (C_0). Data is compiled from 3 independent experiments, data points where C was below the limit of detection for each plaque assay are indicated by open symbols. Dotted line indicates no decay. **C)** Immunofluorescence images of A549 cells infected with IAV samples treated at pH 4 or 7 for 10 or 30 seconds. All samples were neutralized prior to cell infections. A549 cells were infected at a multiplicity of infection (MOI) of 2, and IAV protein production was visualized by immunofluorescent staining of nucleoprotein (NP) at 3 hours post-infection. Scale bar corresponds to 250 µm. Images representative of duplicate experiments. **D)** VSV particles encoding Renilla Luciferase were pseudotyped with HA and NA of the A/WSN/33 virus (VSV-H1N1), for comparison to VSV expressing the wild-type surface protein G (VSV-G). Both VSV stocks were acidified to pH 4, and samples were neutralized after 10 or 30 sec of pH exposure. Control samples of each VSV strain were held at pH 7. Entry capacity of treated VSV samples was then determined by measuring the luciferase activity 7 hours post infection in MDCK cells. Data was derived from 3 independent experiments, with samples quantified in duplicate. Data is presented as $\log_{10}$ of relative light units (RLU) at each time point relative to RLU of non-treated samples (RLU_0). Dotted line indicates no decay. **E)** IAV particles were pH-treated and neutralized as in C, then stained with an HA-specific antibody recognizing the post-fusion HA conformation (purple). Staining with an NP-specific antibody (blue) served as a control to ensure the same amount of viral material was deposited between samples. Scale bar corresponds to 250 µm. Images representative of duplicate experiments.

Transient acidic exposure induces localized conformational changes in external IAV protein haemagglutinin (HA).

Data in **Figure 1** suggested that the loss of IAV infectivity in the pH 4 aerosol condition was due to a conformation change of HA into its post-fusion form. To map specific regions of HA affected by exposure to acidic pH, we used HDX-MS with whole viruses. For this, intact IAV particles were rapidly acidified to pH 4 in bulk solution and exposed for either 10 or 30 seconds, then neutralized back to pH 7. Control samples were mock-adjusted to pH 7 and held in these neutral conditions for the same time-frame, ensuring salt content and sample dilution remained consistent. Neutralized and control samples were then incubated in D_2O buffer on ice for a dedicated time before H/D exchange reactions were rapidly quenched, and viruses lysed with a urea and formic acid treatment. Samples were immediately spun at 4ºC to pellet membranes and debris prior to flash freezing and storage at -80ºC of sample supernatants. This process was designed to retain the whole virus in its near native conformation during pH treatment, neutralization, and subsequent D_2O incubation (schematic shown in **Fig. 2A**).

The HA protein is present as a homotrimer on the surface of IAV, with a membrane-embedded region and internal region that anchors the protein to the viral capsid. Each HA monomer is also comprised of two subunits, HA1 and HA2, connected by a relatively flexible hinge region. IAV in the neutral pH 7 condition was first used to characterize the global D_2O incorporation levels of this surface-exposed glycoprotein. HA showed an alternance of fast- and slow-exchanging regions, suggesting the presence of dynamic and more structured regions (**Fig. 2B**). Peptide coverage was high for the HA1 region and much reduced for membrane-associated HA2 region. Reduced coverage for the HA2 region has also been observed in prior HDX-MS studies analyzing X-31 HA on whole viruses (48,49). Overall, 74% of residues within HA1 and 30% of those within HA2 of A/WSN/33 were effectively covered by our whole-virus HDX-MS analysis (**Supplementary Fig. S2**). Peptides analyzed in our study showed good correlation in their deuteration levels with previous study of IAV HA by HDX-MS (48), with the same alternance in high- and low- exchanging regions being mapped despite use of different virus strains.

Following characterization of HA dynamics at neutral pH, H/D exchange rates after transient pH 4 treatment of the whole virus were characterized. Virus samples were pre-treated at pH 4 or at pH 7 for reference samples, for 10 or 30 seconds, then neutralized back to pH 7 prior to D_2O incubations. Careful tests were run to make sure acid-treated and pH 7-treated samples had the exact same pH following neutralization to avoid differences in H/D exchange rate due to shifts in pH during deuteration. Three different D_2O incubation times (30 sec, 300 sec, 3,600 sec) were used to allow detection of pH-induced changes that occur in highly flexible as well as in more structured regions. Comparison between the conditions mapped several peptides displaying increased exchange rates

following acid treatment (**Fig 2C**, **Supplementary Table S3**). Regions with increased H/D exchange rates were detected after both 10 and 30 seconds of pH 4 treatment. Neutralization of all samples prior to HDX-MS ensured these detected pH-induced changes were non-reversible, and thus are likely to indicate the state of the HA protein on whole IAV after re-inhalation and neutralization of an acidified aerosol on the mucus membrane of a new host.

Six discrete peptides showed differences between the two pH conditions, 5 of which were localized within the HA1 chain. The first identified peptide was from residue 51-58 (Peptide 1 in **Figure 2D**). H/D exchange rates for this peptide after 30 seconds of D_2O incubation were comparable between pH conditions (pH 4 vs 7), though significant differences emerged after longer D_2O exposures of 300 and 3,600 seconds. This peptide is located within the fusion domain (F') of the HA1 subunit. Elevated deuterium incorporation here after pH 4 treatment is likely due to disruption of stabilizing contacts between this domain and the proximally located HA2 subunit [reported in (54)] as the protein transitions to the post-fusion conformation. Peptide 5 (residues 317-328) is located in the same fusion region, and shows a similar enhancement of H/D exchange post-pH 4 treatment.

Peptides 2 (residues 81-92) and 3 (residues 89-95) are overlapping, though show a differential kinetic in H/D exchange suggesting that the 80-90 region is more dynamic than the 90-95 region. These observations were not anticipated as the high-resolution X-ray crystal structure of HA [PDB: 1RU7 from (55)] suggests the presence of an α-helix in the 80-90 region, which was expected to be more protected from H/D exchange than the unstructured 90-95 region (**Fig. 2E**). Peptide 4 (residues 113-117) lies in the vestigial esterase (E′) subdomain of HA1 and spans an alpha-helical region and loops. The highly significant increase in H/D exchange rate observed at every D_2O incubation times suggest that the secondary structure element might unfold upon pH 4 treatment. Peptide 4 is also buried within the center of the HA homotrimer in the pre-fusion conformation, making close contact with the β-loop of the HA2 subunit. In the post-fusion confirmation, the RBD of HA1 is rotated away from the central stalk (49,56), releasing contact with HA2 and leaving these previously protected peptides more exposed to the external environment.

Peptide 6 (residues 521-532) sits immediately prior to the anchoring transmembrane region of HA2. During transition to post-fusion HA, this membrane proximal region is reported to become disordered (56), which is in-line with the large increase in H/D exchange rate observed after pH 4 exposure. A similar increase in H/D exchange within the C-terminal region of HA for the H3N2 IAV strain X-31 was also observed post-fusion by Garcia *et al*. (48). Interestingly, we observed one peptide within HA showing EX1 or bimodal distribution (residue 402-418, corresponding to the β-loop, addressed in the next section).

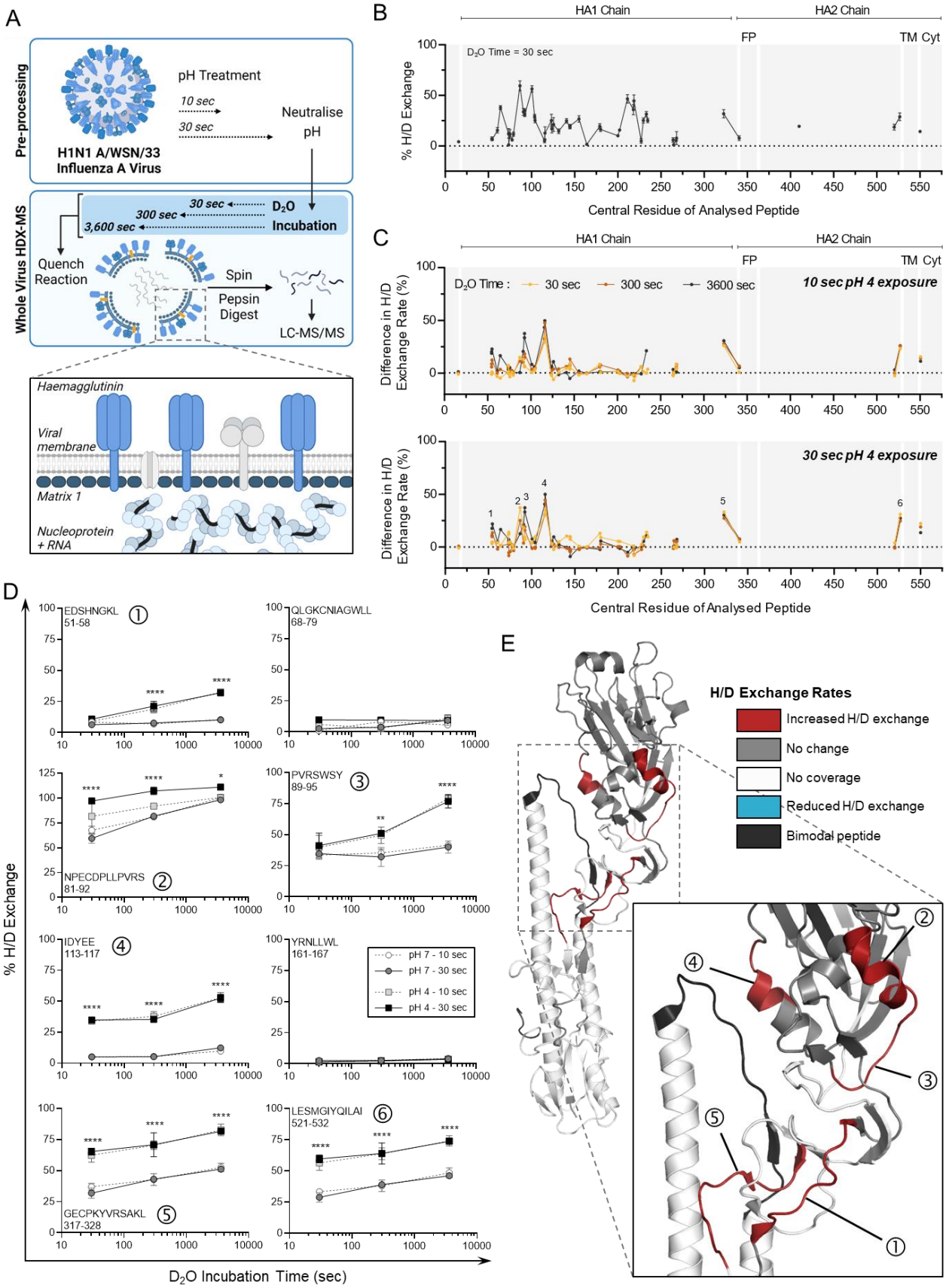
A
Pre-processing
pH Treatment
10 sec
30 sec
Neutralise pH
H1N1 A/WSN/33 Influenza A Virus
Whole Virus HDX-MS
30 sec
300 sec
3,600 sec
D2O Incubation
Quench Reaction
Spin
Pepsin Digest
LC-MS/MS
Haemagglutinin
Viral membrane
Matrix 1
Nucleoprotein + RNA
B
HA1 Chain
HA2 Chain
FP
TM Cyt
D2O Time = 30 sec
% H/D Exchange
Central Residue of Analysed Peptide
C
D2O Time :
30 sec
300 sec
3600 sec
10 sec pH 4 exposure
30 sec pH 4 exposure
Difference in H/D Exchange Rate (%)
Central Residue of Analysed Peptide
D
% H/D Exchange
EDSHNGKL 51-58
QLGKCNIAGWLL 68-79
NPECDPLLPVRS 81-92
PVRSWSY 89-95
IDYEE 113-117
YRNLLWL 161-167
GECPKYVRSAKL 317-328
LESMGIYQILAI 521-532
pH 7 - 10 sec
pH 7 - 30 sec
pH 4 - 10 sec
pH 4 - 30 sec
D2O Incubation Time (sec)
E
H/D Exchange Rates
Increased H/D exchange
No change
No coverage
Reduced H/D exchange
Bimodal peptide

Figure 2 – HDX-MS characterization of HA protein from whole IAV after transient exposure to acidic conditions. A) Schematic of the whole-virus HDX-MS process. In bulk solution, whole virus is held at neutral pH or is acidified at pH 4 for 10 or 30 seconds prior to neutralizing back to pH 7. Neutralized whole-virus samples are incubated in D_2O buffer for 30, 300, or 3,600 seconds, then quenched, prior to pepsin digestion and LC-MS analysis. Organization of viral proteins within the intact influenza A virion are highlighted by the inset, with the external Haemagglutinin (HA), and the internal proteins Matrix 1 (M1) and Nucleoprotein (NP) colored blue for visibility. **B)** Hydrogen/deuterium (H/D) exchange percentages measured for HA protein from whole IAV samples held at neutral conditions (pH 7) for 30 seconds. Samples were then incubated in D_2O for 30 seconds, quenched, and digested prior to HDX-MS analysis. Data points indicate the mean percentage of H/D exchange ± SD for triplicate samples. Peptides are organized linearly according to the position of the central amino acid of each individual peptide along the published sequence for HA (Uniprot: P03452). Continuous lines indicate regions of continuous peptide coverage by MS. Peptides showing bimodal activity are excluded from the graph. Protein domains of interest are indicated by grey shading and white lines; FP = fusion peptide, TM = transmembrane domain, Cyt = cytoplasmic region. **C)** Residual plots showing the difference in H/D exchange percentages induced by exposure to pH 4 for 10 seconds or 30 seconds, when compared to corresponding pH 7 control samples. Individual data points indicate the mean percentage of H/D exchange difference for triplicate samples. Dotted line indicates no difference in H/D exchange. Peptides of interest showing increased H/D exchange are numbered 1 – 6. **D)** Uptake plots for Peptides 1-6 showing increased H/D exchange after pH 4 exposure. Data shows the total percentage of H/D exchange for pH 7 or 4 samples after D_2O incubation for 30, 300, or 3,600 seconds. The sequence and residue positions of each peptide are indicated in each panel. Data points indicate the mean percentage of H/D exchange ± SD for triplicate samples. Data analyzed by Two-way ANOVA (** $p < 0.01$, *** $p < 0.001$, **** $p < 0.0001$, when comparing 30 second pH-exposed samples for each D_2O time-point. Statistical results for comparison of 10 second pH-exposed samples appear in **Supplementary Table S1**). **E)** Protein regions showing increased (red) or decreased (blue) H/D exchange rates, or showing no change in H/D exchange rates (grey) after 30 seconds at pH 4 (compared to pH 7 control) mapped onto the crystal structure of A/PR8 HA (PDB: 1RU7). White indicates regions of no peptide coverage, and peptides with bimodal activity are colored black. HA monomer is shown, with inset showing the location of peptides 1-5. Peptide 6 (521-532) does not appear as the crystal structure is truncated prior to these residues.

Peptide bimodal distribution is induced by acidic exposure for the β-loop of HA protein.

One peptide (HA2, 402-418) showing bimodal H/D exchange behavior after both pH 7 and pH 4 treatments was detected, suggesting the presence of distinct populations with different conformations. This peptide is located within the β-loop of the HA2 subunit, as indicated in **Figure 3A**. This is one of the primary regions known to modify its conformation in pH-triggered HA, changing from a flexible loop to a stabilized α-helix. When in neutral conditions, unimodal H/D exchange was initially detected. Representative spectra in **Figure 3B** show the mass shift and fraction of each population for the 402-418 peptide after a 30 second deuterium incubation, with a single peak indicating unimodal distribution for pH 7 samples. A second population (orange) then became distinguishable after longer D_2O incubation times, indicating bimodal distribution, though these two peaks were mostly overlapping for the entire D_2O incubation period (up to 1 hour) for pH 7 controls. Conversely, following pH 4 treatment of the whole virus, the bimodal distribution was observed even after short D_2O incubation times. The second peak was also more deuterated than in pH 7 samples. For peptides showing bimodal distribution, also referred as EX1 kinetics, deconvolution analysis was applied to quantify the fraction of each population (**Fig. 3C**).

Bimodal exchange behavior is indicative of the presence of two distinct conformations, with long-range allosteric rearrangements occurring upon transiting from one state to another. Benhaim *et al.* (49) reported a similar observation for the HA β-loop of the H3N2 strain X-31 after rapid acidification at pH 5 at a host-temperature of 37°C. Their study showed appearance of an intermediate and highly deuterated peak after ~1 minute of pH exposure, which progressively disappeared to be overtaken by a highly protected segment as pH exposure progressed.

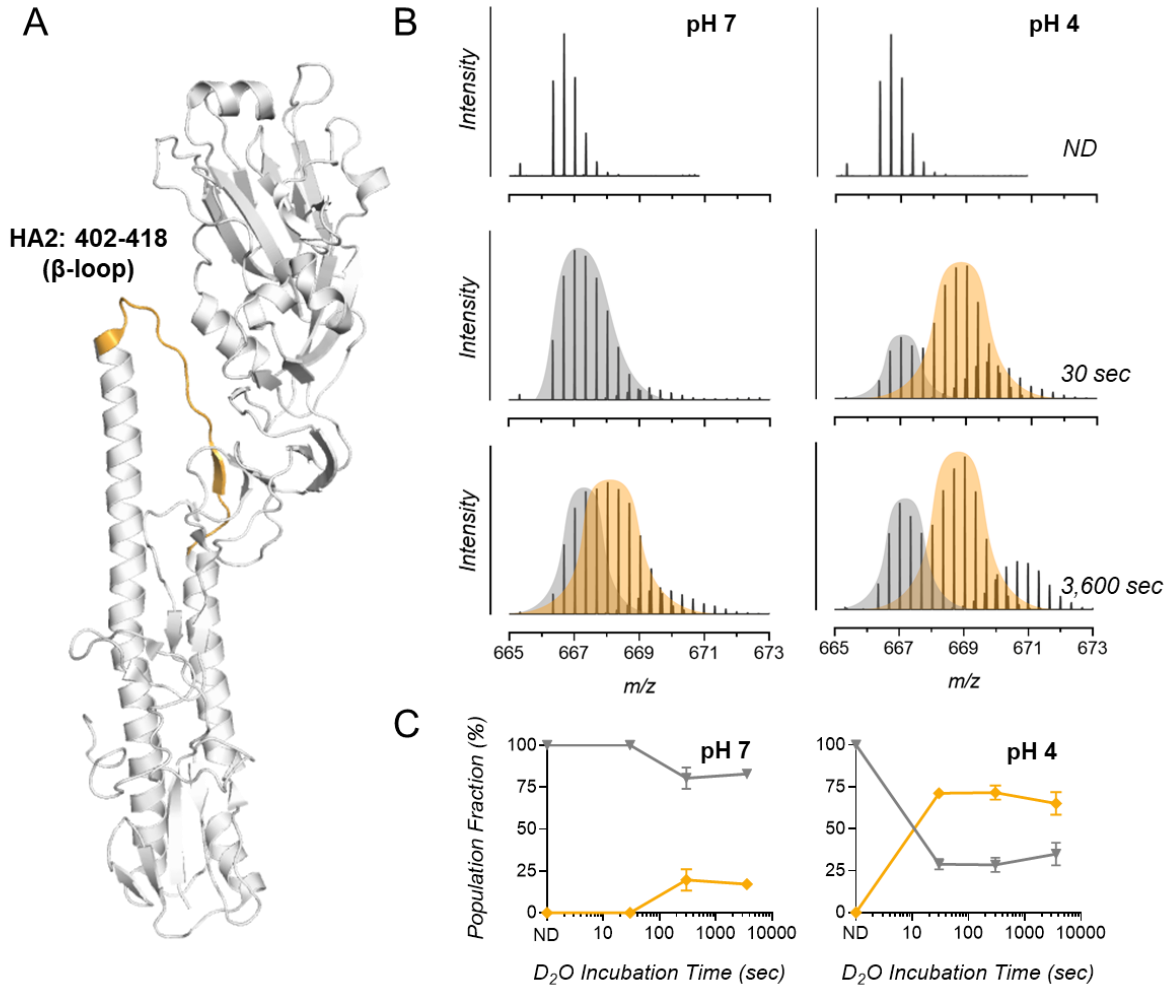

Figure 3 – Regions of bimodal H/D exchange within IAV HA identified by whole virus HDX-MS. Whole virus samples were pH adjusted to 4, then neutralized back to pH 7 after 30 seconds. Following pH neutralization, samples were incubated in D_2O buffer for 30, 300, or 3,600 seconds, prior to quench, digestion, and processing for HDX-MS analysis. Control samples were held at pH 7 for 30 seconds prior to D_2O incubations and HDX-MS. **A)** HDX-MS analysis revealed the HA peptide 402 – 418 (part of the HA2 subunit) displayed bimodal activity, and this peptide is highlighted orange on the crystal structure of A/PR8 HA (PDB: 1RU7). **B)** Representative spectra of triplicate samples from pH 7 and pH 4 groups showing a mass shift for bimodal peptide 402 – 418 with increasing D_2O incubation times. Mass shift is compared to samples incubated in non-deuterated buffer (ND). Bimodal envelopes are separated by grey and orange coloring. **C)** Proportions of the left (grey) and right (orange) populations are graphed with time. Data indicates the mean ± SD for triplicate samples analyzed by HDX-MS.

Transient exposure to low pH has limited effect on viral capsids, genome integrity, and lipid content.

In addition to monitoring conformational changes on the surface-exposed HA trimeric protein, we wondered whether structural integrity of virus particles and genomic material was affected when whole IAV was pH-exposed. We suspected additional mechanisms of inactivation may be occurring as HA conformational changes observed by HDX-MS were very similar upon 10- or 30-seconds pH 4 exposure, though infectious titers continued to drop. To this end, the structure of the viral capsid was assessed. TEM imaging showed that IAV in neutral conditions was spherical/ovoid, with virions being relatively well dispersed across the grid (**Fig. 4A**). Spikes of HA were also readily visible and well organized across the viral surface. In contrast, after exposing the virus to pH 4 (30 seconds) and neutralizing back to pH 7, virions were somewhat aggregated, and those appearing as single particles or smaller clusters had reduced structural integrity. Most noticeably, the organization of HA spikes on the surface of individual virions was compromised after pH 4 treatment, providing additional evidence that HA had undergone an irreversible conformational change following transient acidic exposure. The post-fusion HA trimeric complex is known to expose hydrophobic regions within the HA2 stem that are buried pre-fusion (57–59). Increased hydrophobicity of virions due to HA conformation change is likely to mediate the aggregation of whole viral particles observed here in pH 4 samples. It is important to note that our prior work has established that viral aggregation is not the driver of infectious titer loss in our system (30). Some virions also appeared to be in the process of lysis by TEM, though overall, most viral particles appeared structurally intact after pH 4 treatment.

Viral capsid integrity was additionally quantified by an assay utilizing RNase treatment and genome quantification by RT-qPCR. Whole viral samples were exposed to pH 4 or pH 7 for 30 seconds, prior to neutralization back to pH 7. Then, neutralized samples were split in 2 groups; one was treated with RNase, and the second was mixed with PBS (no RNase) before incubation of both at 37°C for 30 min. Then, all samples were subject to viral RNA extraction and quantification by RT-qPCR. Samples with no RNase treatment showed comparable genome amplification regardless of pH pre-treatment (**Fig. 4B**), indicating the segment of the IAV genome amplified here was not affected by pH alone. For samples that were mixed with RNase, we observed varying levels of amplifiable RNA copies. Copies in PBS and pH 7 control samples did not drop significantly after RNase treatment, indicating the amplified genome segment was sufficiently protected from degradation by an intact viral capsid. Conversely, pH 4-treated samples showed a significant loss of amplifiable genome after RNase exposure, suggesting that some viral capsids were no longer intact to protect the genome from RNase-mediated degradation. Overall, the drop in total genome copies was approximately 2-$\log_{10}$ for pH 4-treated samples in 30 seconds. Whilst significant, this is not the same magnitude of titer decrease observed for infectivity (upwards of 5-$\log_{10}$ loss of viral titer in the same time-frame), indicating that loss of capsid integrity is likely to be contributing to viral inactivation, but is not the primary driver.

It was also of interest to see if pH treatment could affect the lipid classes within the IAV lipid envelope. IAV lipid membranes are typically rich in sterols and sphingolipids, and are depleted in lipids with a glycerol backbone (e.g. glycerophospholipids) compared with the cell membranes these viruses typically bud from (60). Here, we measured the relative abundance of 500 lipid species using liquid chromatography/mass spectrometry (LC/MS) untargeted lipidomics, after whole-virus exposure to pH 4, 5, or 7 for 30 seconds followed by neutralization. Data in **Supplementary Figure S3** shows no significant change in lipid levels upon pH 4 or pH 5 treatment over the time-frame of interest. While key lipids (i.e., sterols) have not been considered here, and future work will assess potential lipid alterations in more detail, data indicates there are no major alterations to the lipid envelope composition after pH exposure. Thus, loss of lipid integrity is unlikely to be contributing to aerosol-associated virus inactivation. TEM imaging (**Fig. 4A**) also showed no obvious disintegration of the lipid envelope post-pH exposure.

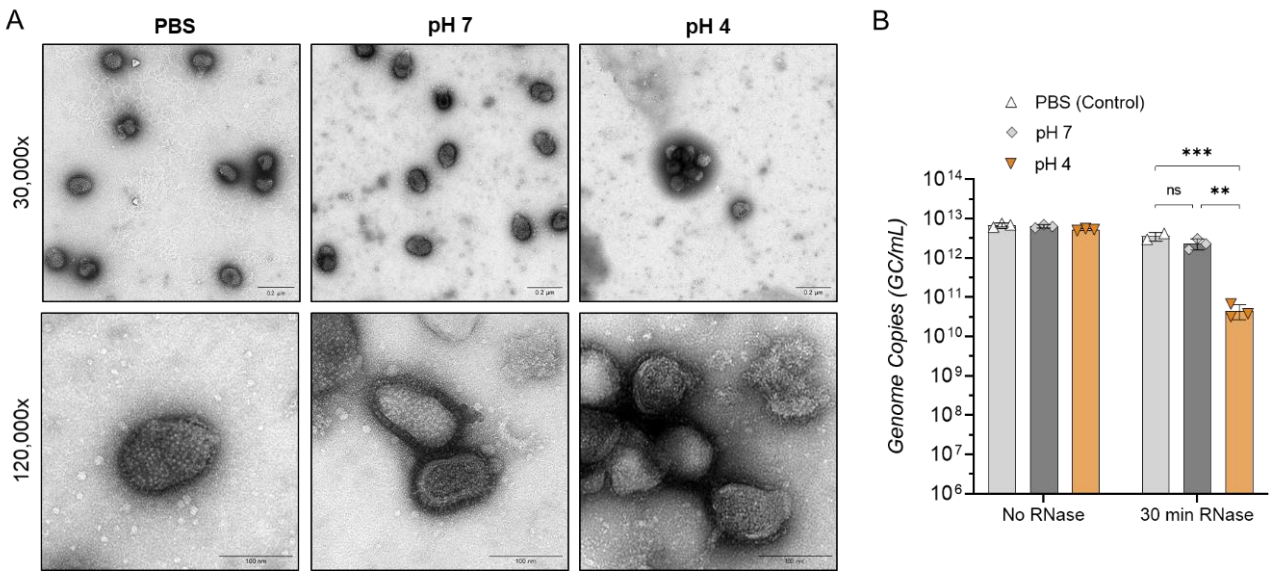

Figure 4 – Effect of aerosol pH on IAV structural integrity. IAV was adjusted to pH 4, then neutralized back to pH 7 after 30 seconds of exposure at room-temperature. Control samples were mock-adjusted to pH 7 for the same time period, or were suspended in PBS only. **A)** Neutralized and control samples were fixed in PFA, then stained with 2% uranyl acetate and imaged using the Tecnai Spirit TEM (imaged at 30,000x and 120,000x magnification). Images are representative of duplicate samples. **B)** Alternatively, neutralized virus samples were incubated in the presence of RNase or PBS (no RNase control) prior to RNA extraction and genome quantification by RT-qPCR. Data presented as mean genome copies/mL ± SD for triplicate samples. Data analyzed by Two-Way ANOVA (** $p < 0.01$, *** $p < 0.001$, ns not significant).

Ambient acidic exposure has no effect on internal nucleoprotein (NP).

As some viral capsids were ruptured as a result of pH treatment, it was of interest to determine whether the internal protein NP was affected. At baseline (neutral conditions, pH 7), NP showed a number of inherently flexible regions, particularly towards the C-terminal end of the protein (**Fig. 5A**). When comparing pH 7 to pH 4 treated samples however, no significant changes in H/D exchange rates were detected for any peptides within NP, indicating no conformational changes or localized unfolding were occurring (**Fig. 5B – C, Supplementary Table S4**). This protein gave the highest coverage percentage of all three studied, with 75% of the entire sequence covered by at least one peptide (**Supplementary Fig. S4**). It cannot be excluded that non-covered regions show pH-induced conformational changes and this could be the focus of follow-up work. However, NP is tightly complexed with viral RNA in a helical-like quaternary structure, thus high stability during acid treatment is expected. Additionally, quantification of RNA copies in pH 4- or pH 5-treated viruses by RT-qPCR showed no loss of signal intensity for the amplified genome region, even after 30 min of acidic exposure (**Fig. 5D**). Another section of the IAV genome has previously been shown to be very pH stable even down to a gastric acid pH of 2. Authors found that whilst viral infectivity could be rapidly depleted in simulated gastric acid, RNA copy numbers were found to be stable for prolonged incubation (at least 4 hours) in these conditions (61). Thus, structural damage to NP and/or to IAV genome segments are unlikely contribute to the loss of viral infectivity observed in acidic aerosol conditions.

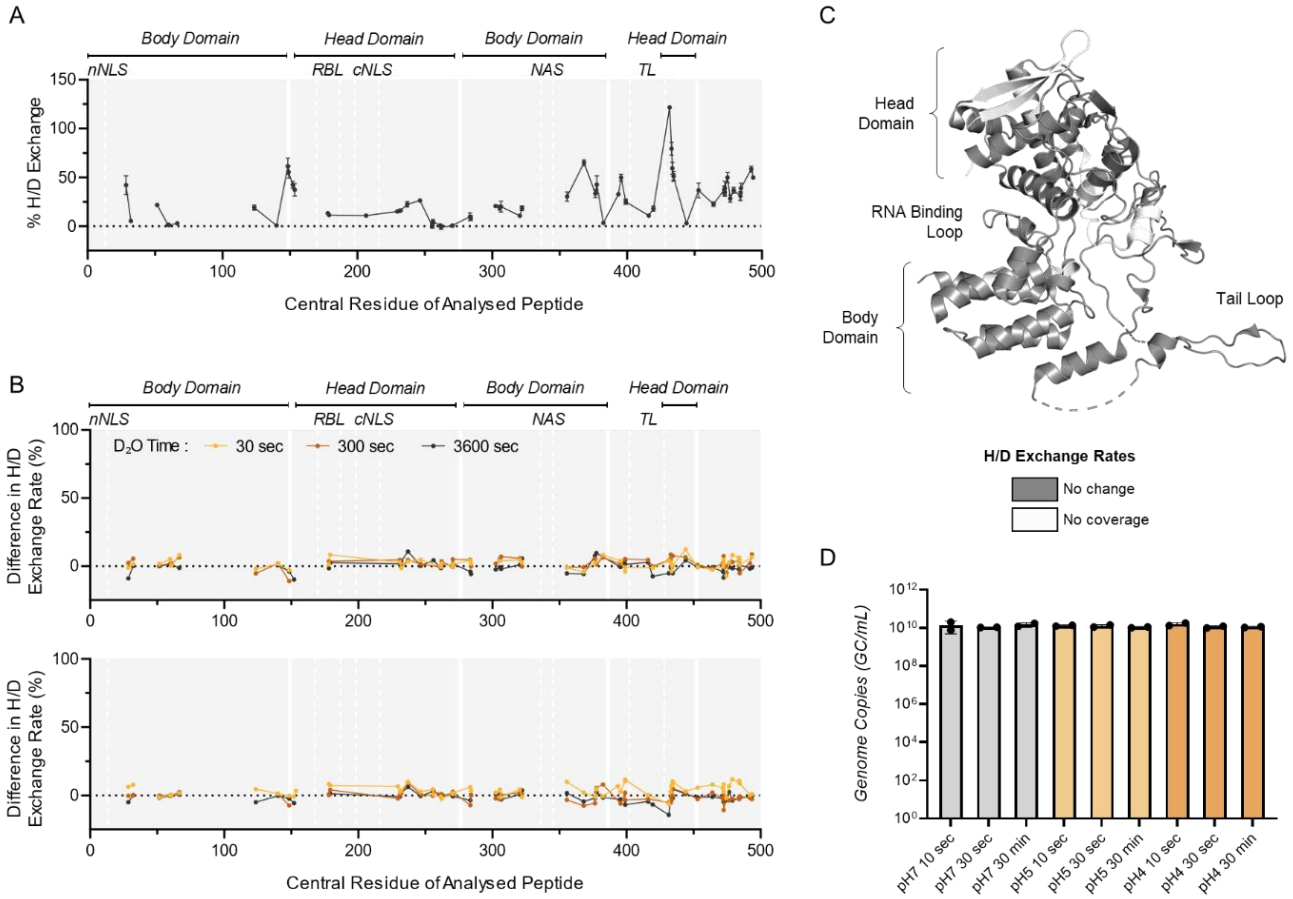

Figure 5 – HDX-MS characterization of NP protein from whole IAV after transient exposure to acidic conditions. A) Hydrogen/deuterium (H/D) exchange percentages measured for NP protein from whole IAV samples held at neutral conditions (pH 7) for 30 seconds. Samples were then incubated in D_2O for 30 seconds, quenched, and digested prior to HDX-MS analysis. Data points indicate the mean percentage of H/D exchange ± SD for each peptide plotted using its central amino acid (n=3, Uniprot: P03466). Continuous lines indicate regions of continuous peptide coverage by MS. Protein domains of interest are indicated by grey shading and white lines; nNLS = non-conventional nuclear localization signal, RBL = RNA binding loop, cNLS = conventional nuclear localization signal, NAS = nuclear accumulation signal, TL = tail loop. **B)** Whole virus samples were pH adjusted to 4, then neutralized back to pH 7 after 10 or 30 seconds. Following pH neutralization, samples were incubated in D_2O buffer for 30, 300, or 3,600 seconds, prior to quench, digestion, and processing for HDX-MS analysis. Control samples were held at pH 7 for 10 or 30 seconds prior to D_2O incubations and HDX-MS. Data presented as residual plots showing the difference in H/D exchange percentages induced by exposure to pH 4 for 10 seconds or 30 seconds, when compared to corresponding pH 7 control samples. Individual data points indicate the mean percentage of H/D exchange difference for triplicate samples. **C)** Crystal structure of A/WSN/33 NP (PDB: 2IQH), showing regions of coverage by HDX-MS. White indicates regions of no peptide coverage by HDX-MS. Head and body domains, along with RNA binding loop and tail loop of NP are annotated based on Ye *et al.* (62). **D)** RT-qPCR results showing the IAV genome region tested (M2 genome segment) is able to be replicated to comparable levels regardless of pH 4, 5 or 7 pre-treatments. Samples were all neutralized back to 7 prior to RNA extraction and RT-qPCR. Data presented as mean genome copies (GC/mL) ± SD for duplicate samples.

Ambient acidic exposure induces C-terminal flexibility in internal protein Matrix 1 (M1).

Due to the partial effect induced on the IAV capsid by pH 4 treatment, we also sought to determine whether the major capsid protein, M1, was structurally altered. M1 is the most abundant structural protein within IAV particles, and oligomerizes to form a 'shell' layer underneath the viral envelope. M1 is an α-helical protein with two major domains; a globular N-terminal domain (NTD), and a comparably unstructured C-terminal domain (CTD), which are connected by a coiled linker sequence (63,64). Exposure of M1 to low pH during virus entry is thought to cause the M1 layer to dissociate, which ultimately allows capsid disassembly and viral genome detachment and release into the host cell cytoplasm (65–67). The M1 conformational changes that accompany this event are substantially less well characterized than those of HA, and whether the rapid and ambient pH exposure used here was sufficient to structurally affect M1 had not yet been determined.

HDX-MS analysis of M1 under neutral conditions (pH 7) revealed a dynamic CTD, in line with the current literature on M1. This was indicated by multiple peptides showing above 50% H/D exchange (**Fig. 6A**). Flexibility of the M1 C-terminus has been documented before, and has been reported to cause issues with resolution of this region using standard crystallographic methods (68). As with HA, the close membrane association of the N-terminal region of the M1 protein caused some coverage limitations, with substantially less peptides generated from the membrane binding domain. Despite this, 68% of the overall M1 protein sequence was covered by at least one unique peptide (**Supplementary Fig. S5**).

H/D exchange rates of peptides in M1 NTD were not affected by pH treatment apart from the loop encompassing residues 128-141 that showed protection from exchange following pH 4 exposure (Peptide 1 in **Fig. 6C**). This was shown for 2 overlapping peptides covering the same region. This observation suggests that this region adopts a more structured conformation upon pH 4 exposure. In agreement with this, prior work comparing X-ray crystal structures of M1 at neutral and acidic conditions indicated that structural differences were negligible within the NTD, apart from a loop centered around residue 135 (63). In sharp contrast, the C-terminal region encompassing alpha-helices H10 to H12 exhibits significantly increased H/D exchange rates post-pH 4 exposure. The results correlate well with past work using small-angle X-ray scattering and atomic force microscopy, which suggested that a low-pH induced conformational change in M1 was most pronounced in the CTD and in the linker region between N and CTDs (68).

Several peptides encompassing residues 202-212 in helix H11 showed a bimodal distribution, which was significantly more pronounced following pH 4 exposure (**Fig. 6E-F**). This H/D exchange regime is reminiscent of long-range conformational changes and suggest that exposure to acidic treatment promotes transition of an alpha-helix to a loop structure. The absence of peptides showing EX1

kinetics in helix H10 and H12, in contrast with neighboring helix H11, may be explained by the more structured conformation of the latter helix. Indeed, helices H10 and H12 have very high deuteration levels after only 30 seconds deuteration, whereas helix H11 is more protected from exchange even after 1-hour incubation in deuterated buffer (**Supplementary Table S5**). The high magnitude of differences in H/D exchange rates observed for the CTD suggest a large unfolding of the alpha-helical structures upon acidic pH treatment, which may disrupt intra-molecular contacts known to exist between the CTD and NTD of neighboring M1 molecules (64) and lead to partial capsid disassembly.

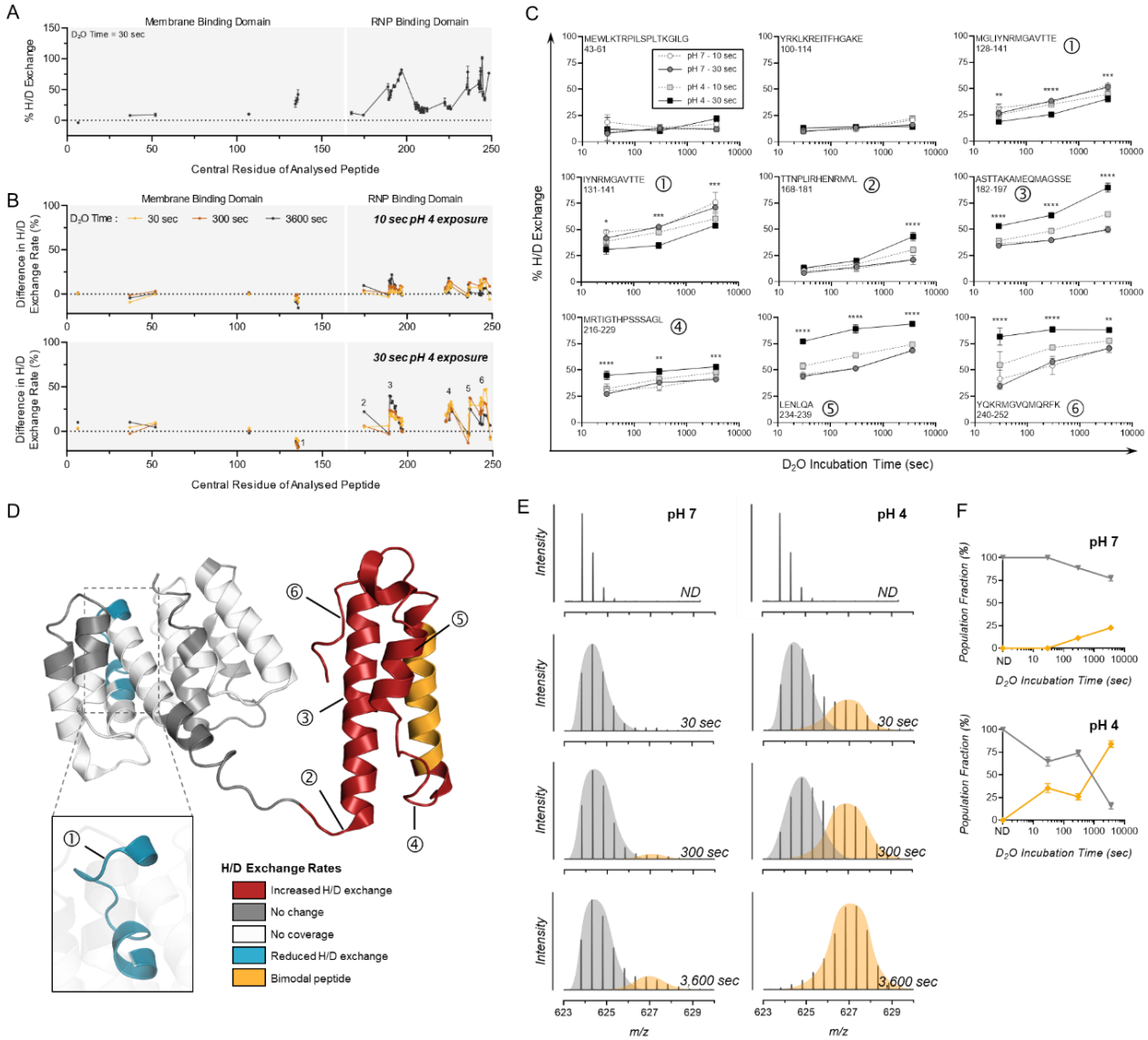

Figure 6 – HDX-MS characterization of M1 protein from whole IAV after transient exposure to acidic conditions. A) Hydrogen/deuterium (H/D) exchange percentages measured for M1 protein from whole IAV samples held at neutral conditions (pH 7) for 30 seconds. Each point shows the mean percentage of H/D exchange ± SD for a peptide represented by its central amino acid number (n=3, Uniprot: P05777). Continuous lines indicate regions of continuous peptide coverage by MS. Membrane binding domain and ribonucleoprotein (RNP) binding domain are indicated by grey shading and white lines. **B)** Data presented as residual plots showing the difference in H/D exchange percentages induced by exposure to pH 4 for 10 seconds or 30 seconds, when compared to corresponding pH 7 control samples. Peptides showing bimodal activity are excluded, unimodal peptides only are presented in panel B. Individual data points indicate the mean percentage of H/D exchange difference for triplicate samples. Peptides of interest showing increased H/D exchange are numbered 1-6. **C)** Uptake plots for Peptides 1-6 showing increased H/D exchange after pH 4 exposure. Data shows the total percentage of H/D exchange for pH 7 or 4 samples after D_2O incubation for 30, 300, or 3600 seconds. The sequence and residue positions of each peptide are indicated in each panel. Data shows points indicate the mean percentage of H/D exchange ± SD for triplicate samples. Data analyzed by Two-way ANOVA (* $p < 0.05$, ** $p < 0.01$, *** $p < 0.001$, **** $p < 0.0001$, when comparing 30 second pH -exposed samples at each D_2O time-point. Statistical results for comparison of 10 second pH-exposed samples appear in **Supplementary Table S2**). **D)** Protein regions showing increased (red) or decreased (blue) H/D exchange rates, or showing no change in H/D exchange rates (grey) after 30 seconds at pH 4 (compared to pH 7 control) mapped onto the crystal structure of A/PR8 M1 (PDB: 7JM3). White indicates regions of no peptide coverage, peptides with bimodal activity are colored orange. **E)** Representative spectra of triplicate samples from pH 7 and pH 4 groups showing a mass shift for bimodal peptide 204-218 with increasing D_2O incubation times. Bimodal peaks are separated by grey and orange coloring. **F)** Proportions of the left (grey) and right (orange) peaks are graphed with time. Data indicates the mean ± SD for triplicate samples analyzed by HDX-MS.

DISCUSSION

Environmental transmission relies on viruses staying infectious long enough to come into contact with the next host. Non-enveloped viruses are typically considered more stable than enveloped viruses (69,70), particularly in aqueous environments (71). Despite this sensitivity, many enveloped viruses do undergo effective environmental transmission, with expelled liquid droplets and aerosols being major transmission vectors for numerous respiratory viruses. Research into factors influencing enveloped virus inactivation or persistence during environmental transmission will help predict transmission risks for newly emerging pathogens, and will inform the design of novel public health strategies.

In this study, we sought to improve understanding of the liquid microenvironment encountered by the human pathogen IAV during environmental transmission through the air. In light of the SARS-CoV-2 pandemic, increasing attention has been given to the expiratory aerosol as a primary carrier of respiratory viruses, including IAV (14–23). Importantly, these aerosols are small enough to remain suspended in room air for prolonged periods of time (as opposed to larger particles which are subject to rapid gravitational settling), they can accumulate in poorly ventilated areas, and can be inhaled by a new host and settle deep within the respiratory tract to establish severe infection (72). Thus, it is important for ongoing respiratory virus control to understand what happens to viruses suspended within fine aerosols, and to identify potential inherent mechanisms of virus inactivation that may be exploited for improved virus control.

Initial modelling of aerosol particles revealed that an acidic pH of 4 is attained after equilibration of expired aerosols of multiple sizes with room air (**Fig 1A**). Low pH has previously been shown to inactivate enveloped phi6 bacteriophage suspended in small droplets, representative of fomite transmission (73). It is well-known that IAV has high sensitivity to acidic pH, thus it was of interest to determine how the acidic aerosol environment would affect viral infectivity, with particular focus on the structural lipid, genome, and protein components. All experiments were performed with whole virus rather than purified molecules to mimic the natural virus setting where many stabilizing protein-protein and protein-lipid interactions are present. Infectivity data showed that whole IAV was highly sensitive to decay in an acidic aerosol environment, with >5-$\log_{10}$ decrease in infectious titers within 30 seconds of low pH exposure. We acknowledge the limitations of this study for determining the effect of low aerosol pH on IAV in combination with other aerosol factors, including the presence of protective proteins, organic components, effect of phase separation during aerosol evaporation, etc. We also recognize that the salt-based pH buffers used here do not reflect the complexity and variability of lung and nasal fluids from human patients, in which IAV would be suspended in a variable aerosol setting. This will be addressed in a future publication, though our prior work has indicated that protective matrix effects are minimized at lower pH (30). Regardless, the aim of the current study was

to decouple the effect of low pH from these other factors (whether inactivating or protective) within an evaporating aerosol, for mechanistic characterization.

Collectively, our whole-virus mass spectrometry data showed that viral proteins rather than lipids were undergoing measurable changes over the time-course relevant to the observed viral decay. HDX-MS data points to the HA (**Fig. 2**) and M1 (**Fig. 6**) proteins as drivers of virus inactivation. The remaining structural proteins of IAV (M2, NA) and the replication associated proteins (PA, PB1, PB2) were at too low of a copy number per virion to analyze using our whole-virus method, and analysis using purified RNP complexes or virus-like particles could be conducted in the future for additional characterization. Viral RNPs have previously been found to aggregate at low pH (~5), though this aggregation was mostly reversed by pH neutralization (74) suggesting no permanent changes occur. The amplified region of the IAV genome was also unaffected in our study by low pH exposure (**Fig. 5D**), and NP, which coats the IAV genome segments, showed no pH-induced conformational changes by HDX-MS analysis (**Fig. 5B – C**). Functionality data also implicated the premature attainment of the post-fusion form of HA as the primary cause of rapid IAV inactivation under acidic aerosol conditions (**Fig. 1C – E**).

It was somewhat unexpected that the HA conformational change would be the principle driver of IAV inactivation. The pH-mediated change of HA is well-documented in the literature, however conditions described to trigger this involve longer and hotter incubations at pH ~5.5, as these are the conditions encountered by the virus within the host cell endosome. Despite the very rapid time scale, the ambient temperature, and the substantially lower pH used here (1.5 pH units below fusion), HA was shown to transition to the post-fusion state, or at the very least was triggered to enter a stable intermediate state that prevents viral attachment and entry. Numerous studies have reported intermediate HA states between pre- and post-fusion (49,75–79), some of which seem to also be reversible (80–82). The retained flexibility and bimodal H/D exchange behavior of the β-loop in particular (**Fig. 3**) indicated that for our pH-exposed samples, HA was in an intermediate state, similar to that shown by HDX-MS data of Benhaim *et al.* (49) for H3N2 HA in early points post-pH exposure.

Importantly, re-neutralization of our samples prior to any HDX-MS analysis indicated an irreversible transition, leading to definitive loss of infectivity after acidification. Additional experiments testing longer exposure times or higher temperatures (37°C as opposed to ambient) would help in classifying the degree of flexibility in the β-loop post-pH exposure in our system. Regardless, it can be concluded that HA rapidly deviates from the pre-fusion form. This physical rearrangement inhibits binding of the virus to its host cell receptor, and is in contrast to key epitopes being chemically damaged by pH 4 exposure. Indeed, residues within the HA globular head that constitute the receptor binding domain (RBD, comprised of the 130-loop, 190-helix, and 220-loop) were not altered in terms of H/D exchange

by pH, suggesting that if HA remained in its pre-fusion conformation, host cell attachment would be unaffected by acidification of an expiratory aerosol.

Changes detected in HA at 10 seconds were not amplified by 30 seconds (**Fig. 2C**), despite viral titers continuing to drop (**Fig. 1B**). Thus, whilst HA appeared to mediate the majority of inactivation, changes to M1 and the associated capsid disassembly could drive additional inactivation. In fact, inactivation kinetics in **Figure 1B** could be classified as two-step kinetics, with a sharp initial drop in infectivity from 0 to 10 seconds post-pH exposure, followed by a slower rate of decay up to 30 seconds. This second portion of inactivation could be attributed to M1 conformational changes and associated capsid disassembly. In cryo-EM studies, incubation of H3N2 IAV at low pH was reported to induce loss of spherical virion morphology and a disruption and/or coiling of the matrix layer away from the viral envelope in some virions only, whilst other virions in the same suspension showed unaffected morphology and a resolvable matrix later (65)(80). This suggest M1 disassembly affects some but not all virions in a population at the same rate. This was similarly observed for H1N1 A/WSN/33 here, with some but not all virions showing loss of spherical morphology by TEM after low pH treatment for 30 seconds (**Fig. 4A**). The capsid integrity assay (**Fig. 4B**) also indicated that lysed viral particles could account for ~2-$\log_{10}$ in viral titer reduction by 30 seconds post-pH exposure. This would supplement the initial sharp 3-$\log_{10}$ reduction seen over the first 10 seconds, which we attribute to HA changes. Whilst the first ~30 seconds of pH exposure was of the most interest here, it could also be beneficial to classify the state of these IAV proteins after longer pH exposure times (e.g. 5 minutes, 30 minutes) in a subsequent study, to assess ongoing changes.

As IAV is able to participate in effective aerosol transmission, there may exist some component (e.g. a protective protein from the lung or nasal environment) that could stabilize HA and/or M1 and reduce acid-mediated conformational changes from occurring in human-derived aerosols. For example, IAV has been demonstrated to readily bind sialic acids present on respiratory mucins (83–85). These mucins are part of the protective mucus layer secreted by epithelial cells of the respiratory tract, and presentation of sialylated glycans by respiratory mucins is intended to act as a decoy receptor for the virus (85,86). This IAV-mucin interaction has also been shown to be weaker than the true IAV-host cell interaction (87) and is often reversible due to the action of viral neuraminidase (83,88). It is feasible that a transient interaction such as this could be stabilizing for viral HA during aerosol transport between hosts In fact, prior publication by our group showed that co-incubation of A/WSN/33 with nasal mucus offered some degree of protection to the virus against pH-mediated decay in bulk solution around pH 5 (30). Hirose *et al.* also demonstrated that IAV and Influenza B virus suspended in simulated gastric acid (pH 2) rapidly lost infectivity, but could be protected from acid-mediated inactivation for at least 4 hours if co-incubated with artificial mucus (61). It will be the focus of a follow-

up study to determine if this protection is due to transient stabilization of HA by mucins against premature formation of post-fusion HA.

Alternatively, as we saw acidification is predicted to be slower for larger aerosol particles by ResAM, it may be that larger aerosol particles are predominant carriers of infectious IAV. Increased times to reach the terminal pH 4 (~ 30 min for a 5 μm particle, **Fig. 1A**) would give the virus ample time to reach a new host before acid-mediated changes could even occur. Respiratory viral genomes have been found to be enriched in fine aerosol particles ≤ 5 μm compared with coarser aerosols in humans (23,33). Infectious IAV was also detected in the fine aerosol fraction but not the coarse fraction (> 5 μm) expelled by humans in Yan *et al.* (23). Whilst not human-specific, ferret-ferret IAV transmission was found to be mediated by airborne particles of 1.5 μm diameter and above. Particles small enough to pass through a 1.0 μm diameter filter from infected ferrets did not cause seroconversion or viral shedding in recipient ferrets, indicating lack of productive infection (89). This may be due to the rapid acidification of the smallest particles, causing IAV inactivation before a new host could be reached. Future studies will be required to establish if the predominant carriers of infectious IAV in humans are aerosols between the discrete range of 1.5 – 5 μm.

It is also of immense interest to determine whether other respiratory viruses (e.g. MERS CoV, rhinovirus, respiratory syncytial virus, etc.) will be similarly affected by acidic aerosol pH, and whether a broad acting air treatment could be employed as a non-pharmaceutical intervention to reduce infectious viral loads in the air. Alternatively, a spray based therapeutic could be utilized to enhance acidification of exhaled aerosols in high-risk settings. A prior study investigated the efficacy of a low pH (~3.5) nasal spray for mitigating the effects of influenza A infection in a ferret model. The nasal sprays tested were based on simple acid mixtures (including L-pyroglutamic acid, succinic acid, citric acid and ascorbic acid), and their topical application to infected ferrets reduced severity of viral-induced symptoms and reduced viral shedding (90). As multiple epitopes on HA were found to be affected by pH here, the non-specificity of low pH to drive IAV inactivation means that this approach may be less prone to resistance development than current antiviral drugs. IAV is also specifically reliant upon acidic pH exposure for progression of its natural infection cycle *in vivo*, thus development of resistance to acidic pH is highly unlikely.

Overall, information gained here improves our understanding of the innate inactivation mechanisms for IAV under indoor aerosol conditions. Whole-virus HDX-MS has only been used previously to characterize the HA protein of H3N2 IAV strain X-31. We have demonstrated protein conformational changes on whole-virus looking at three proteins (HA, M1 and NP) of a different virus strain (H1N1 A/WSN/33), and complemented these protein-based studies with global analyses of whole-virus morphology, RNA material, and lipid integrity. Expanding this body of IAV HDX-MS data to encompass additional strains and subtypes will enable future study of mechanistic

similarities/differences between viral proteins, e.g. in terms of pH susceptibilities of different HA and M1 molecules to predict environmental stability and transmission risks, or to perform comparison of epitope flexibilities to predict efficacy of neutralizing antibodies or antivirals against novel strains. These findings additionally open up novel perspectives for the development of molecules interfering with HA and M1 structure as novel antivirals to inhibit aerosol transmission.

MATERIALS & METHODS

Influenza Virus Stocks. Influenza A virus (IAV) strain A/WSN/33 [H1N1 subtype] was propagated in Madin-Darby Canine Kidney (MDCK) cells (ThermoFisher). Cells were maintained in Dulbecco's modified Eagle's medium (DMEM, Gibco) supplemented with 10% Fetal Bovine Serum (FBS; Gibco), and 1% Penicillin-Streptomycin 10,000 U/mL (P/S; Gibco). Confluent MDCK monolayers were washed and inoculated with IAV at a MOI of 0.001 for 72 h in OptiMEM (Gibco) supplemented with 1% P/S and 1 µg/mL TPCK trypsin (Sigma, T1426). Infected culture supernatants were clarified by centrifugation at 2,500 ×*g* for 10 min, and IAV was then pelleted through a 30% sucrose cushion at 112,400 ×*g* in a SW31Ti rotor (Beckman) or an AH-629 rotor (ThermoFisher Scientific) for 90 min at 4ºC. Pellets were recovered in phosphate buffered saline (PBS, ThermoFisher, 18912014) overnight at 4ºC. Concentrated IAV stocks were quantified at 1.2×10^{10} to 7.5×10^{11} PFU/mL by plaque assay (described below), and at 5 mg/mL total viral protein by Qubit Protein Assay quantification kit (Life Technologies, Q33211).

Recombinant Vesicular Stomatitis Virus (VSV) stocks harboring a Firefly Luciferase gene instead of VSV G (Kerafast, EH1020-PM) were pseudotyped with either the VSV G protein (VSV-G) or the A/WSN/1933 HA and NA (VSV-H1N1). 8×10^5 HEK293T cells/well were seeded into 6-well plates and transfected the next day with ViaFect (Promega, E4981), using either 4 µg of plasmid expressing the G protein or 2 µg of plasmid expressing HA together with 2 µg of plasmid expressing NA. After incubation at 37°C for 24 h, cells were infected with a previously made VSV-G Luc stock at a MOI of 4 in DMEM. After 1.5 h at 37°C cells were washed with PBS and incubated with DMEM containing 1 µg/ml anti-VSV-G antibody (Kerafast, EB0010) for 24 h at 37°C. Note that this was added to the VSV-H1N1 wells only, VSV-G stocks were generated without the antibody. Supernatant was collected and clarified by centrifugation at 300 ×*g* for 5 min. VSV-H1N1 stocks were additionally treated with 5 µg/mL TPCK-treated trypsin (Sigma-Aldrich, T1426) for 20 min at 37°C, followed by trypsin inactivation with 10 µg/ml Soybean Trypsin inhibitor (Sigma-Aldrich, T6522) for 20 min at 37°C. VSV-G and VSV-H1N1 stocks were aliquoted and frozen at -80°C.

Plaque Assay. Plaque assay was conducted using monolayers of MDCK cells in 12-well plates. IAV samples were serially diluted in 'PBS for infections' (PBSi; PBS supplemented with 1% P/S, 0.02 mM Mg^{2+}, 0.01 mM Ca^{2+}, 0.3% bovine serum albumin [BSA, Sigma-Aldrich A1595], final pH ~7.3), before being added to washed cellular monolayers. Viruses were incubated on monolayers for 1 h at 37ºC with 5% CO_2 with manual agitation every 10 min. Non-attached viruses were removed from cells by washing with PBS, and MEM supplemented with 0.5 µg/mL TPCK-trypsin and agarose was added to cells. Infected and control plates were incubated for 72 h at 37ºC with 5% CO_2, and plaques were

visualized after fixing cells in PBS + 10% formaldehyde (Sigma, 47608-1L-F), then staining with 0.2% crystal violet solution (Sigma, HT901-8FOZ) in water + 10% methanol (Fisher Chemical, M-4000-15).

Virus Acidification & Neutralization. Citric acid-Na_2HPO_4 pH buffers were made according to the Sigma Aldrich Buffer Reference System (accessed here: https://www.sigmaaldrich.com/CH/en/technical-documents/protocol/protein-biology/protein-concentration-and-buffer-exchange/buffer-reference-center#citric). Citric acid powder (Acros Organics, 220345000) and Na_2HPO_4 powder (Fluka Chemika, 71640) were dissolved in miliQ H_2O to reach concentrations of 0.1 M and 0.2 M respectively. 0.1 M citric acid and 0.2 M Na_2HPO_4 solutions were then mixed together as specified in the Sigma Aldrich Reference System to generate 1× pH 4 or 7 buffers. Alternatively, concentrated 1M citric acid and 2 M Na_2HPO_4 solutions were made, and mixed in the same ratios to generate 10× pH 4 or 7 buffers. For IAV infectivity analysis, 1× pH buffers were used to pH adjust virus samples. Purified IAV was spiked ~1/100 into 1× pH 4 or pH 7 buffers (final concentration 1×10^7 PFU/mL or 1×10^8 PFU/mL), vortexed briefly to mix, and left to incubate at ambient temperature. At specified time-points, a sample was taken and diluted 1/100 in PBSi to neutralize pH. Alternatively, samples were neutralized by a 1/10 dilution in PBSi containing 3% 10× pH 7 buffer to minimize virus dilution. pH testing ensured both dilution methods neutralized the pH to above 6.7 – 7.0 in all cases. Neutralized samples were frozen prior to titration by plaque assay or fluorescence assay.

For HDX-MS, lipid-MS, VSV analyses, TEM imaging, and RNase Capsid Integrity Assay, 10× pH buffers were used to adjust purified virus samples to pH 4 or 7, by adding 10× pH buffers to the virus sample in a 1:9 ratio. This strategy allowed pH to be finely tuned whilst keeping virus sample concentrations as high as possible. For example, to adjust to pH 4, 1 µL of acidification buffer (10× pH 4.0 buffer, comprised of 600 mM citric acid, 800 mM Na_2HPO_4) was added to 9 µL of virus sample, and vortexed for 2 seconds to mix. This reduces sample pH from ~7.3 to 4.0. To neutralize IAV samples, 2.2 µL of 2M Na_2HPO_4 was added to the 10 µL mixture of acidified virus, and vortexed for 2 seconds to mix. Note that mixing non-adjusted virus with 2M Na_2HPO_4 in the same ratio did not impact IAV infectious titers (**Supplementary Fig. S6**). To neutralize VSV samples, acidified VSV was diluted 1/10 in PBSi containing 3% 10× pH 7 buffer. Both neutralization methods restored pH to a neutral pH of 6.7 to 7.0. For neutral control samples, 1 µL of 10× pH 7.2 buffer (160 mM citric acid, 1.68 M Na_2HPO_4) was mixed with 9 µL of virus sample and vortexed for 2 seconds to mix, as a mock acidification. This reduced sample pH from ~7.3 to 7.0. To mock neutralize, 2.2 µL of 10× pH 7.0 buffer (130.5 mM citric acid, 1.74 M Na_2HPO_4) was added to this 10 µL and vortexed for 2 seconds to mix. This retained pH at 7.0, and this strategy ensured salt concentrations and virus concentrations were comparable between neutralized pH 4 and pH 7 samples prior to downstream analysis. All pH adjustments and incubations were performed at ambient room temperature (22 – 25°C).

VSV Infectivity Analysis. To measure inactivation of pseudotyped VSV, samples were acidified and neutralized as described above and subsequently tested for entry capacity by measuring the luciferase activity of infected MDCK cells. To do so, 3×10^4 cells/well were seeded into 96-well plates and incubated overnight. The next day, cells were washed and infected with 50 µL of neutralized VSV sample for 1.5 h at 37°C. Cells were washed with PBS and incubated in DMEM with 10% FBS and 1% P/S. Luciferase activity was quantified 7 hours post infection using the ONE-Glo Luciferase Assay System (Promega, E6110) in combination with the PerkinElmer EnVision plate reader.

Fluorescence Imaging of Infected Cells & Viral Particles. IAV samples were acidified and neutralized as described above, resulting in final concentrations of 1×10^7 PFU/mL. Samples were then used for infection and subsequent staining of intracellular NP or direct staining of viral particles. To evaluate virus entry after acidification, A549 cells were infected for 1 h at 37°C with neutralized IAV diluted in PBSi at a multiplicity of infection (MOI) of 2 (calculated from titers prior to acidification). Afterwards, cells were washed with PBS and incubated for 2 or 5 h in DMEM supplemented with P/S, 0.2% BSA, 20 mM HEPES (Sigma-Aldrich, H7523) and 0.1% FBS. Infected cells were fixed for 15 min with 3.7% formaldehyde (ThermoFisher Scientific, 26908) in PBS and subsequently blocked and permeabilized for 1 h at RT in PBS supplemented with 50 mM ammonium chloride (Sigma-Aldrich, 254134), 0.1% saponin (Sigma-Aldrich, 47036), and 2% BSA (Sigma-Aldrich, A7906). Primary murine monoclonal anti-NP antibody (hybridoma supernatant, ATCC, HB-65) was applied for 1 h at RT (or overnight at 4°C when required). Cells were washed in PBS, and bound primary antibody was detected using anti-mouse IgG Alexa488 (ThermoFisher Scientific, A-11029). Infected cells were also stained with DAPI (Sigma-Aldrich, 10236276001) and incubated at RT for 1 h.

To analyze HA conformation of viral particles, 150 µL of neutralized IAV was centrifuged onto cover slips for 30 min at 1000 ×*g*. Virus samples were then fixed, blocked, and permeabilized as described above, and IAV was stained using a murine monoclonal post-fusion HA antibody (hybridoma supernatant, Wistar - Coriell Institute, Y8-10C2) and a rabbit polyclonal anti-NP antibody (kind gift of J. Pavlovic, Institute of Medical Virology, Zurich, Switzerland). Samples were washed in PBS, and bound antibodies were detected using anti-mouse IgG Alexa546 (ThermoFisher Scientific, A-11031) and anti-rabbit IgG Alexa488 (ThermoFisher Scientific, A-11008). Following washing in PBS, cover slips were mounted with ProLong Gold Antifade Mountant (Thermo Fisher Scientific, P36930). Stained slides and cells were imaged with the SP8 confocal laser scanning microscope (Leica) or the DMi8 microscope (Leica) in combination with the THUNDER Instant Computational Clearing algorithm (Leica).

Transmission Electron Microscopy. Purified IAV samples were pH-adjusted and neutralized using 10× pH buffers as described above. All samples were pH exposed for 30 seconds at ambient room

temperature prior to neutralization. Neutralized samples were then diluted to 10^{10} PFU/mL equivalent in 1× pH 7.0 buffer and fixed with 0.06% paraformaldehyde for 4 days at 4°C prior to use in TEM. 5 µL of each fixed sample was deposited onto carbon-coated copper grids (Electron Microscopy Sciences, CF400-Cu). Grids were UV-glow discharged immediately prior to sample addition, and sample was left to adsorb for 2 min at room temperature. Excess solution was blotted using Whatman filter paper, and grids were washed in a droplet of miliQ water. Samples were then negatively stained for 1 min with 5 µL of 2% uranyl acetate (Electron Microscopy Sciences, 541-09-3. Excess stain was blotted, and grids were allowed to air dry for 5 min. Grids were imaged using the Tecnai Spirit TEM (spot size: 2, emission: 4.41 uA, accelerating voltage: 80 kV).

RNase Assay for Capsid Integrity. IAV samples were pH-adjusted and neutralized as described above, using 1× pH buffers. Samples were pH exposed for 30 seconds at ambient room temperature prior to neutralization. As a control, virus was mixed with PBS only and held at ambient temperature. Neutralized and control whole-virus samples were then diluted 1/100 into RNase digestion mixture (TE buffer with 10 mM Tris and 1 mM EDTA [Invitrogen, AM9858], supplemented with 50 mM NaCl, pH adjusted to 7.0 and with HCl. RNase A/T1 [Thermo-Scientific, EN0551] then added for 40 µg/mL RNase A and 100 U/mL T1 final concentrations). Samples vortexed to mix, and statically incubated at 37°C for 30 min. As controls, identical neutralized samples were diluted 1/100 into control digestion mixture (PBS added to TE buffer in the absence of RNase A/T1), vortexed, and incubated alongside RNase-treated samples. After 30 min, SUPERase-In RNase Inhibitor (Invitrogen, AM2694, acts against RNase A, B, C, 1, T1) was added to all samples, and incubated at room temperature for 20 min Samples were then frozen at -20°C overnight prior to RNA extraction using the QIAamp Viral RNA Mini extraction kit (Qiagen, 52906) according to manufacturer's instructions. Viral RNA was stored at -80°C until analysis.

RT-qPCR. Amplification and detection were performed using the One Step PrimeScript™ RT-PCR Kit (RR064A, Takara Bio) with the following primers targeting the IAV M segment:

Forward primer 5'-ATGAGYCTTYTAACCGAGGTCGAAACG-3'

Reverse primer 5'-TGGACAAANCGTCTACGCTGCAG-3'

The RT-qPCR mixture for IAV detection was 7.5 µL of 2× One-Step SYBR RT-PCR Buffer, 0.3 µL of Takara Ex Taq HS (5 U/µL stock), 0.3 µL PrimeScript RT enzyme mix, 0.3 µL forward and reverse primers (10 uM stocks), 3.3 µL RNase-free water, and 3 µL extracted RNA sample. All sample manipulations were performed under biosafety cabinets, and the following conditions were used for the one-step cycling program: 5 min at 95°C for denaturation, followed by 40 cycles of 95°C for 5 sec, 60°C for 20 sec, and 72°C for 10 sec for annealing and extension. For quantification, we created a standard curve using a titration of a Gblock gene fragment, as described in (91). All RT-qPCR reactions were performed in duplicate, and each PCR run contained non-template controls which

were always negative. Sample dilutions ensured no PCR inhibition in our experimental protocol. Reactions were measured using a Mic Real-Time PCR System from Bio Molecular Systems.

ResAM Modelling. The multi-layer Respiratory Aerosol Model (ResAM) simulates the composition and pH changes inside an expiratory particle following exhalation and subsequent equilibration with room air (for a detailed description of the viral study with ResAM, see (30)). The model performs calculations for particles of selectable size (from 20 nm to 1 mm) with a liquid phase composed of organic and inorganic species representative of human respiratory fluids, specifically synthetic lung fluid. Conditions of indoor room air were set at 20°C and 50% relative humidity, with concentrations of 36.3 ppb NH_3, 0.27 ppb HNO_3, and 600 ppm CO_2, as described in the above study.

Hydrogen-Deuterium exchange coupled to Mass-Spectrometry (HDX-MS). Purified IAV samples were pH-adjusted and neutralized as described above with 10× pH buffers. Samples were pH exposed for 10 or 30 seconds at ambient room temperature prior to neutralization. To initiate HDX, neutralized whole-virus samples were incubated in D_2O buffer (99% deuterium oxide, Sigma 151882, supplemented with 120 mM NaCl). 40 µL D_2O buffer was added to every 10 µL of neutralized virus (final D_2O concentration 78%) on ice for 30 seconds, 300 seconds, or 3,600 seconds in triplicate. After each D_2O incubation, samples were quenched by dilution into ice-cold quench buffer (miliQ containing 150 mM tris(2-carboxyethyl) phosphine-HCl [TCEP, Thermo-Scientific, PG82080], 2 M urea [Sigma, U5128], and 0.1% formic acid [FA, Acros Organics, 270480280] final concentrations, pH 2.5). Samples were spun at 21,000 ×*g* for 2 min in a pre-cooled 4ºC centrifuge, and supernatant was immediately flash-frozen in liquid nitrogen then stored at -80ºC until analysis by HDX-MS. Non-deuterated (ND) controls were prepared identically using pH 7 and pH 4 neutralized virus, using H_2O supplemented with 120 mM NaCl instead of D_2O.

Deuterium incorporation quantification. To quantify deuterium uptake into the protein, protein samples were thawed and injected in UPLC system immersed in ice. The protein was digested via two immobilized pepsin columns (Thermo, 23131), and peptides were collected onto a VanGuard precolumn trap (Waters). The trap was subsequently eluted and peptides separated with a C18, 300Å, 1.7 µm particle size Fortis Bio column 100 x 2.1 mm over a gradient of 8 – 30 % buffer B over 20 min at 150 µL/min (Buffer A: 0.1% formic acid; buffer B: 100% acetonitrile). Mass spectra were acquired on an Orbitrap Velos Pro (Thermo), for ions from 400 to 2200 m/z using an electrospray ionization source operated at 300 °C, 5 kV of ion spray voltage. Peptides were identified by data-dependent acquisition after MS/MS and data were analyzed by Mascot. Deuterium incorporation levels were quantified using HD examiner software (Sierra Analytics), and quality of every peptide that was checked manually. Results are presented as percentage of theoretical maximal deuteration levels. Extended results are found in Supplementary Tables S3, S4 and S5. Changes in deuteration level between two states were considered significant if >12% and >0.6Da and $p<0.05$ (unpaired t-test).

Whole Virus Lipid Mass Spectrometry. Purified IAV samples were diluted to 8×10^{10} PFU/mL in PBS, then pH-adjusted and neutralized after 30 seconds of pH exposure at ambient temperature, as described above. Neutralized whole-virus samples were then diluted 1/100 in chloroform:methanol (1:1 mixture) using glass pipettes, in 2 mL Eppendorf Safe-Lock Polypropylene tubes. Samples were briefly vortexed to mix, and kept at 4ºC until analysis. Lipid extracts were separated over an 8-minute gradient at a flow rate of 200 µL/min on a HILIC Kinetex Column (2.6lm, 2.1×50 mm^2) on a Shimadzu Prominence UFPLC xr system (Tokyo, Japan). Mobile phase A was acetonitrile:methanol 10:1 (v/v) containing 10 mM ammonium formate and 0.5% formic acid, while mobile phase B was deionized water containing 10 mM ammonium formate and 0.5% formic acid. The elution gradient began at 5% B at 200 µL/min and increased linearly to 50% B over 7 min, held at 50% B for 1.5 min, and finally, the column was re-equilibrated for 2.5 min. MS data were acquired in full-scan mode at high resolution on a hybrid Orbitrap Elite (Thermo Fisher Scientific, Bremen, Germany). The system was operated at 240,000 resolution (*m/z* 400) with an AGC set at 1.0E6 and one microscan set at 10-ms maximum injection time. The heated electrospray source HESI II was operated in positive mode at 90 °C and a source voltage at 4.0KV. Sheath gas and auxiliary gas were set at 20 and 5 arbitrary units, respectively, while the transfer capillary temperature was set to 275 °C.

Mass spectrometry data were acquired with LTQ Tuneplus2.7SP2 and treated with Xcalibur 4.0QF2 (Thermo Fisher Scientific). Lipid identification was carried out with Lipid Data Analyzer II (LDA v. 2.6.3, IGB-TUG Graz University) (92). The LDA algorithm identifies peaks by their respective retention time, *m/z* and intensity. Care was taken to calibrate the instrument regularly to ensure a mass accuracy consistently lower than 3 ppm thereby leaving only few theoretical possibilities for elemental assignment. Data visualization was improved with LCMSexplorer in a homemade web tool hosted at EPFL.

Statistical Analysis. Quantitative results expressed as mean ± SD. Student's t-test was used for comparison of data from 2 groups, One-way ANOVA used for comparison of data from 3 or more groups involving a single independent variable, Two-way ANOVA used when data was grouped according to two independent variables. Tukey's multiple comparisons test used for post-hoc analysis. All analyses performed using GraphPad Prism, version 9.4.0 (GraphPad Software, La Jolla, USA). P-values <0.05 (95% confidence) considered statistically significant.

Acknowledgements. We thank Rémy Visentin and Alexandre Hainard from the protein and proteomics platforms at the University of Geneva for assistance with HDX-MS sample acquisition. We thank Davide Demurtas of the EPFL Interdisciplinary Centre for Electron Microscopy (CIME) for assistance with TEM imaging. We also acknowledge the following funding sources supporting this research: a SNSF Sinergia Grant awarded to TK, UK, AN, and SS (Grant #189939).

Competing Interests' Statement. The authors state they have no competing interests or disclosures.

Data Availability Statement. All data relating to this study will be shared in accordance with FAIR (findable, accessible, interoperable, and reusable) data principles, and data will be deposited in the community-approved and cross-disciplinary public repository Zenodo, upon acceptance of publication. The mass spectrometry proteomics data have been deposited to the ProteomeXchange Consortium via the PRIDE partner repository (93) with the dataset identifier PXD037176.

REFERENCES

1. Leung NHL, Chu DKW, Shiu EYC, Chan KH, McDevitt JJ, Hau BJP, et al. Respiratory virus shedding in exhaled breath and efficacy of face masks. Nat Med. 2020 May;26(5):676–80.
2. Lednicky JA, Lauzard M, Fan ZH, Jutla A, Tilly TB, Gangwar M, et al. Viable SARS-CoV-2 in the air of a hospital room with COVID-19 patients. Int J Infect Dis. 2020 Nov;100:476–82.
3. Kutter JS, de Meulder D, Bestebroer TM, Lexmond P, Mulders A, Richard M, et al. SARS-CoV and SARS-CoV-2 are transmitted through the air between ferrets over more than one meter distance. Nat Commun. 2021 Mar 12;12(1):1653.
4. Santarpia JL, Herrera VL, Rivera DN, Ratnesar-Shumate S, Reid SP, Ackerman DN, et al. The size and culturability of patient-generated SARS-CoV-2 aerosol. J Expo Sci Environ Epidemiol. 2021 Aug 18;1–6.
5. Li Y, Qian H, Hang J, Chen X, Cheng P, Ling H, et al. Probable airborne transmission of SARS-CoV-2 in a poorly ventilated restaurant. Build Environ. 2021 Jun;196:107788.
6. Lednicky JA, Lauzardo M, Alam MM, Elbadry MA, Stephenson CJ, Gibson JC, et al. Isolation of SARS-CoV-2 from the air in a car driven by a COVID patient with mild illness. Int J Infect Dis. 2021 Jul;108:212–6.
7. Viklund E, Kokelj S, Larsson P, Nordén R, Andersson M, Beck O, et al. Severe acute respiratory syndrome coronavirus 2 can be detected in exhaled aerosol sampled during a few minutes of breathing or coughing. Influenza and Other Respiratory Viruses. 2022;16(3):402–10.
8. Fabian P, Brain J, Houseman EA, Gern J, Milton DK. Origin of exhaled breath particles from healthy and human rhinovirus-infected subjects. J Aerosol Med Pulm Drug Deliv. 2011 Jun;24(3):137–47.
9. Dick EC, Jennings LC, Mink KA, Wartgow CD, Inhorn SL. Aerosol transmission of rhinovirus colds. J Infect Dis. 1987 Sep;156(3):442–8.
10. Myatt TA, Johnston SL, Rudnick S, Milton DK. Airborne rhinovirus detection and effect of ultraviolet irradiation on detection by a semi-nested RT-PCR assay. BMC Public Health. 2003 Jan 13;3:5.
11. Myatt TA, Johnston SL, Zuo Z, Wand M, Kebadze T, Rudnick S, et al. Detection of airborne rhinovirus and its relation to outdoor air supply in office environments. Am J Respir Crit Care Med. 2004 Jun 1;169(11):1187–90.
12. Kulkarni H, Smith CM, Lee DDH, Hirst RA, Easton AJ, O'Callaghan C. Evidence of Respiratory Syncytial Virus Spread by Aerosol. Time to Revisit Infection Control Strategies? Am J Respir Crit Care Med. 2016 Aug 1;194(3):308–16.
13. Tseng CC, Chang LY, Li CS. Detection of airborne viruses in a pediatrics department measured using real-time qPCR coupled to an air-sampling filter method. J Environ Health. 2010 Nov;73(4):22–8.
14. Tellier R. Review of Aerosol Transmission of Influenza A Virus. Emerg Infect Dis. 2006 Nov;12(11):1657–62.
15. Tellier R. Aerosol transmission of influenza A virus: a review of new studies. J R Soc Interface. 2009 Dec 6;6 Suppl 6:S783-790.
16. Wong BCK, Lee N, Li Y, Chan PKS, Qiu H, Luo Z, et al. Possible role of aerosol transmission in a hospital outbreak of influenza. Clin Infect Dis. 2010 Nov 15;51(10):1176–83.
17. Koster F, Gouveia K, Zhou Y, Lowery K, Russell R, MacInnes H, et al. Exhaled aerosol transmission of pandemic and seasonal H1N1 influenza viruses in the ferret. PLoS One. 2012;7(4):e33118.
18. Noti JD, Lindsley WG, Blachere FM, Cao G, Kashon ML, Thewlis RE, et al. Detection of infectious influenza virus in cough aerosols generated in a simulated patient examination room. Clin Infect Dis. 2012 Jun;54(11):1569–77.
19. Cowling BJ, Ip DKM, Fang VJ, Suntarattiwong P, Olsen SJ, Levy J, et al. Aerosol transmission is an important mode of influenza A virus spread. Nat Commun. 2013 Jun 4;4(1):1935.
20. Bischoff WE, Swett K, Leng I, Peters TR. Exposure to influenza virus aerosols during routine patient care. J Infect Dis. 2013 Apr;207(7):1037–46.

21. Lindsley WG, Noti JD, Blachere FM, Thewlis RE, Martin SB, Othumpangat S, et al. Viable Influenza A Virus in Airborne Particles from Human Coughs. Journal of Occupational and Environmental Hygiene. 2015 Feb 1;12(2):107–13.
22. Pan M, Bonny TS, Loeb J, Jiang X, Lednicky JA, Eiguren-Fernandez A, et al. Collection of Viable Aerosolized Influenza Virus and Other Respiratory Viruses in a Student Health Care Center through Water-Based Condensation Growth. mSphere. 2017 Oct;2(5):e00251-17.
23. Yan J, Grantham M, Pantelic J, Mesquita PJB de, Albert B, Liu F, et al. Infectious virus in exhaled breath of symptomatic seasonal influenza cases from a college community. PNAS. 2018 Jan 30;115(5):1081–6.
24. Alford RH, Kasel JA, Gerone PJ, Knight V. Human Influenza Resulting from Aerosol Inhalation. Proceedings of the Society for Experimental Biology and Medicine. 1966 Jul 1;122(3):800–4.
25. Little JW, Gordon RD, Hall Jr. WJ, Roth FK. Attenuated influenza produced by experimental intranasal inoculation. Journal of Medical Virology. 1979;3(3):177–88.
26. Marr LC, Tang JW, Van Mullekom J, Lakdawala SS. Mechanistic insights into the effect of humidity on airborne influenza virus survival, transmission and incidence. Journal of The Royal Society Interface. 2019 Jan 31;16(150):20180298.
27. van Doremalen N, Bushmaker T, Morris DH, Holbrook MG, Gamble A, Williamson BN, et al. Aerosol and Surface Stability of SARS-CoV-2 as Compared with SARS-CoV-1. N Engl J Med. 2020 Apr 16;382(16):1564–7.
28. Smither SJ, Eastaugh LS, Findlay JS, Lever MS. Experimental aerosol survival of SARS-CoV-2 in artificial saliva and tissue culture media at medium and high humidity. Emerg Microbes Infect. 2020 Dec;9(1):1415–7.
29. Dabisch P, Schuit M, Herzog A, Beck K, Wood S, Krause M, et al. The influence of temperature, humidity, and simulated sunlight on the infectivity of SARS-CoV-2 in aerosols. Aerosol Science and Technology. 2021 Feb 1;55(2):142–53.
30. Luo B, Schaub A, Glas I, Klein LK, David SC, Bluvshtein N, et al. Acidity of expiratory aerosols controls the infectivity of airborne influenza virus and SARS-CoV-2 [Internet]. medRxiv; 2022 [cited 2022 Aug 17]. p. 2022.03.14.22272134. Available from: https://www.medrxiv.org/content/10.1101/2022.03.14.22272134v2
31. Oswin HP, Haddrell AE, Otero-Fernandez M, Mann JFS, Cogan TA, Hilditch TG, et al. The dynamics of SARS-CoV-2 infectivity with changes in aerosol microenvironment. Proceedings of the National Academy of Sciences. 2022 Jul 5;119(27):e2200109119.
32. Klein LK, Luo B, Bluvshtein N, Krieger UK, Schaub A, Glas I, et al. Expiratory aerosol pH is determined by indoor room trace gases and particle size. Proceedings of the National Academy of Sciences. 2022 Sep 27;119(39):e2212140119.
33. Gralton J, Tovey ER, McLaws ML, Rawlinson WD. Respiratory virus RNA is detectable in airborne and droplet particles. J Med Virol. 2013 Dec;85(12):2151–9.
34. Fennelly KP. Particle sizes of infectious aerosols: implications for infection control. Lancet Respir Med. 2020 Sep;8(9):914–24.
35. Yang W, Elankumaran S, Marr LC. Concentrations and size distributions of airborne influenza A viruses measured indoors at a health centre, a day-care centre and on aeroplanes. J R Soc Interface. 2011 Aug 7;8(61):1176–84.
36. Milton DK, Fabian MP, Cowling BJ, Grantham ML, McDevitt JJ. Influenza Virus Aerosols in Human Exhaled Breath: Particle Size, Culturability, and Effect of Surgical Masks. PLoS Pathog. 2013 Mar 7;9(3):e1003205.
37. Lindsley WG, Blachere FM, Thewlis RE, Vishnu A, Davis KA, Cao G, et al. Measurements of airborne influenza virus in aerosol particles from human coughs. PLoS One. 2010 Nov 30;5(11):e15100.
38. Guttman M, Lee KK. Isotope Labeling of Biomolecules: Structural Analysis of Viruses by HDX-MS. Methods Enzymol. 2016;566:405–26.
39. Marcsisin SR, Engen JR. Hydrogen exchange mass spectrometry: what is it and what can it tell us? Anal Bioanal Chem. 2010 Jun 1;397(3):967–72.
40. Hebling CM, Morgan CR, Stafford DW, Jorgenson JW, Rand KD, Engen JR. Conformational analysis of membrane proteins in phospholipid bilayer nanodiscs by hydrogen exchange mass spectrometry. Anal Chem. 2010 Jul 1;82(13):5415–9.

41. Zhang Z, Kim CS, Kleinstreuer C. Water Vapor Transport and Its Effects on the Deposition of Hygroscopic Droplets in a Human Upper Airway Model. Aerosol Science and Technology. 2006 Jan 1;40(1):1–16.
42. Wang L, Lane LC, Smith DL. Detecting structural changes in viral capsids by hydrogen exchange and mass spectrometry. Protein Science. 2001;10(6):1234–43.
43. Lanman J, Lam TT, Emmett MR, Marshall AG, Sakalian M, Prevelige PE. Key interactions in HIV-1 maturation identified by hydrogen-deuterium exchange. Nat Struct Mol Biol. 2004 Jul;11(7):676–7.
44. Monroe EB, Kang S, Kyere SK, Li R, Prevelige PE. Hydrogen/deuterium exchange analysis of HIV-1 capsid assembly and maturation. Structure. 2010 Nov 10;18(11):1483–91.
45. Wang L, Smith DL. Capsid structure and dynamics of a human rhinovirus probed by hydrogen exchange mass spectrometry. Protein Science. 2005;14(6):1661–72.
46. Veesler D, Khayat R, Krishnamurthy S, Snijder J, Huang RK, Heck AJR, et al. Architecture of a dsDNA viral capsid in complex with its maturation protease. Structure. 2014 Feb 4;22(2):230–7.
47. Bush DL, Monroe EB, Bedwell GJ, Prevelige PE, Phillips JM, Vogt VM. Higher-Order Structure of the Rous Sarcoma Virus SP Assembly Domain. J Virol. 2014 May;88(10):5617–29.
48. Garcia NK, Guttman M, Ebner JL, Lee KK. Dynamic changes during acid-induced activation of influenza hemagglutinin. Structure. 2015 Apr 7;23(4):665–76.
49. Benhaim MA, Mangala Prasad V, Garcia NK, Guttman M, Lee KK. Structural monitoring of a transient intermediate in the hemagglutinin fusion machinery on influenza virions. Sci Adv. 2020 Apr 29;6(18):eaaz8822.
50. Zayas G, Chiang MC, Wong E, MacDonald F, Lange CF, Senthilselvan A, et al. Cough aerosol in healthy participants: fundamental knowledge to optimize droplet-spread infectious respiratory disease management. BMC Pulm Med. 2012 Mar 21;12:11.
51. Lindsley WG, Blachere FM, Beezhold DH, Thewlis RE, Noorbakhsh B, Othumpangat S, et al. Viable influenza A virus in airborne particles expelled during coughs versus exhalations. Influenza Other Respir Viruses. 2016 Sep;10(5):404–13.
52. Roche S, Bressanelli S, Rey FA, Gaudin Y. Crystal Structure of the Low-pH Form of the Vesicular Stomatitis Virus Glycoprotein G. Science. 2006 Jul 14;313(5784):187–91.
53. Yewdell JW, Gerhard W, Bachi T. Monoclonal anti-hemagglutinin antibodies detect irreversible antigenic alterations that coincide with the acid activation of influenza virus A/PR/834-mediated hemolysis. J Virol. 1983 Oct;48(1):239–48.
54. Rosenthal PB, Zhang X, Formanowski F, Fitz W, Wong CH, Meier-Ewert H, et al. Structure of the haemagglutinin-esterase-fusion glycoprotein of influenza C virus. Nature. 1998 Nov;396(6706):92–6.
55. Gamblin SJ, Haire LF, Russell RJ, Stevens DJ, Xiao B, Ha Y, et al. The structure and receptor binding properties of the 1918 influenza hemagglutinin. Science. 2004 Mar 19;303(5665):1838–42.
56. Benton DJ, Gamblin SJ, Rosenthal PB, Skehel JJ. Structural transitions in influenza haemagglutinin at membrane fusion pH. Nature. 2020 Jul;583(7814):150–3.
57. Gaudin Y, Ruigrok RWH, Brunner J. Low-pH induced conformational changes in viral fusion proteins: implications for the fusion mechanism. Journal of General Virology. 1995;76(7):1541–56.
58. Skehel JJ, Bayley PM, Brown EB, Martin SR, Waterfield MD, White JM, et al. Changes in the Conformation of Influenza Virus Hemagglutinin at the pH Optimum of Virus-Mediated Membrane Fusion. Proceedings of the National Academy of Sciences of the United States of America. 1982;79(4):968–72.
59. Ruigrok RW, Aitken A, Calder LJ, Martin SR, Skehel JJ, Wharton SA, et al. Studies on the structure of the influenza virus haemagglutinin at the pH of membrane fusion. J Gen Virol. 1988 Nov;69 (Pt 11):2785–95.
60. Gerl MJ, Sampaio JL, Urban S, Kalvodova L, Verbavatz JM, Binnington B, et al. Quantitative analysis of the lipidomes of the influenza virus envelope and MDCK cell apical membrane. Journal of Cell Biology. 2012 Jan 16;196(2):213–21.

61. Hirose R, Nakaya T, Naito Y, Daidoji T, Watanabe Y, Yasuda H, et al. Mechanism of Human Influenza Virus RNA Persistence and Virion Survival in Feces: Mucus Protects Virions From Acid and Digestive Juices. The Journal of Infectious Diseases. 2017 Jul 1;216(1):105–9.
62. Ye Q, Krug RM, Tao YJ. The mechanism by which influenza A virus nucleoprotein forms oligomers and binds RNA. Nature. 2006 Dec;444(7122):1078–82.
63. Arzt S, Baudin F, Barge A, Timmins P, Burmeister WP, Ruigrok RW. Combined results from solution studies on intact influenza virus M1 protein and from a new crystal form of its N-terminal domain show that M1 is an elongated monomer. Virology. 2001 Jan 20;279(2):439–46.
64. Peukes J, Xiong X, Erlendsson S, Qu K, Wan W, Calder LJ, et al. The native structure of the assembled matrix protein 1 of influenza A virus. Nature. 2020 Nov;587(7834):495–8.
65. Calder LJ, Wasilewski S, Berriman JA, Rosenthal PB. Structural organization of a filamentous influenza A virus. Proc Natl Acad Sci U S A. 2010 Jun 8;107(23):10685–90.
66. Fontana J, Steven AC. At Low pH, Influenza Virus Matrix Protein M1 Undergoes a Conformational Change Prior to Dissociating from the Membrane. J Virol. 2013 May;87(10):5621–8.
67. Li S, Sieben C, Ludwig K, Höfer CT, Chiantia S, Herrmann A, et al. pH-Controlled Two-Step Uncoating of Influenza Virus. Biophys J. 2014 Apr 1;106(7):1447–56.
68. Shtykova EV, Baratova LA, Fedorova NV, Radyukhin VA, Ksenofontov AL, Volkov VV, et al. Structural Analysis of Influenza A Virus Matrix Protein M1 and Its Self-Assemblies at Low pH. PLOS ONE. 2013 Dec 16;8(12):e82431.
69. Firquet S, Beaujard S, Lobert PE, Sané F, Caloone D, Izard D, et al. Survival of Enveloped and Non-Enveloped Viruses on Inanimate Surfaces. Microbes Environ. 2015 Jun;30(2):140–4.
70. Mahl MC, Sadler C. Virus survival on inanimate surfaces. Can J Microbiol. 1975 Jun;21(6):819–23.
71. Silverman AI, Boehm AB. Systematic Review and Meta-Analysis of the Persistence of Enveloped Viruses in Environmental Waters and Wastewater in the Absence of Disinfectants. Environ Sci Technol. 2021 Nov 2;55(21):14480–93.
72. Wang CC, Prather KA, Sznitman J, Jimenez JL, Lakdawala SS, Tufekci Z, et al. Airborne transmission of respiratory viruses. Science. 2021 Aug 27;373(6558):eabd9149.
73. Lin K, Schulte CR, Marr LC. Survival of MS2 and Φ6 viruses in droplets as a function of relative humidity, pH, and salt, protein, and surfactant concentrations. PLOS ONE. 2020 Dec 8;15(12):e0243505.
74. Zoueva OP, Bailly JE, Nicholls R, Brown EG. Aggregation of influenza virus ribonucleocapsids at low pH. Virus Research. 2002 May 10;85(2):141–9.
75. Doms RW, Helenius A, White J. Membrane fusion activity of the influenza virus hemagglutinin. The low pH-induced conformational change. J Biol Chem. 1985 Mar 10;260(5):2973–81.
76. Stegmann T, White JM, Helenius A. Intermediates in influenza induced membrane fusion. EMBO J. 1990 Dec;9(13):4231–41.
77. Böttcher C, Ludwig K, Herrmann A, van Heel M, Stark H. Structure of influenza haemagglutinin at neutral and at fusogenic pH by electron cryo-microscopy. FEBS Lett. 1999 Dec 17;463(3):255–9.
78. Markosyan RM, Melikyan GB, Cohen FS. Evolution of Intermediates of Influenza Virus Hemagglutinin-Mediated Fusion Revealed by Kinetic Measurements of Pore Formation. Biophysical Journal. 2001 Feb 1;80(2):812–21.
79. Gao J, Gui M, Xiang Y. Structural intermediates in the low pH-induced transition of influenza hemagglutinin. PLOS Pathogens. 2020 Nov 30;16(11):e1009062.
80. Fontana J, Cardone G, Heymann JB, Winkler DC, Steven AC. Structural Changes in Influenza Virus at Low pH Characterized by Cryo-Electron Tomography. Journal of Virology. 2012 Mar 15;86(6):2919–29.
81. Leikina E, Ramos C, Markovic I, Zimmerberg J, Chernomordik LV. Reversible stages of the low-pH-triggered conformational change in influenza virus hemagglutinin. EMBO J. 2002 Nov 1;21(21):5701–10.
82. Xu R, Wilson IA. Structural Characterization of an Early Fusion Intermediate of Influenza Virus Hemagglutinin. Journal of Virology. 2011 May 15;85(10):5172–82.
83. Cohen M, Zhang XQ, Senaati HP, Chen HW, Varki NM, Schooley RT, et al. Influenza A penetrates host mucus by cleaving sialic acids with neuraminidase. Virology Journal. 2013 Nov 22;10(1):321.

84. Groth SFDS. Nasal mucus and influenza viruses. I. The haemagglutinin inhibitor in nasal secretions. Epidemiology & Infection. 1952 Dec;50(4):471–90.
85. Matrosovich M, Klenk HD. Natural and synthetic sialic acid-containing inhibitors of influenza virus receptor binding. Reviews in Medical Virology. 2003;13(2):85–97.
86. de Vries E, Du W, Guo H, de Haan CAM. Influenza A Virus Hemagglutinin–Neuraminidase–Receptor Balance: Preserving Virus Motility. Trends in Microbiology. 2020 Jan 1;28(1):57–67.
87. Kaler L, Iverson E, Bader S, Song D, Scull MA, Duncan GA. Influenza A virus diffusion through mucus gel networks. Commun Biol. 2022 Mar 22;5(1):1–9.
88. Yang X, Steukers L, Forier K, Xiong R, Braeckmans K, Reeth KV, et al. A Beneficiary Role for Neuraminidase in Influenza Virus Penetration through the Respiratory Mucus. PLOS ONE. 2014 Oct 15;9(10):e110026.
89. Zhou J, Wei J, Choy KT, Sia SF, Rowlands DK, Yu D, et al. Defining the sizes of airborne particles that mediate influenza transmission in ferrets. Proceedings of the National Academy of Sciences. 2018 Mar 6;115(10):E2386–92.
90. Rennie P, Bowtell P, Hull D, Charbonneau D, Lambkin-Williams R, Oxford J. Low pH gel intranasal sprays inactivate influenza viruses in vitro and protect ferrets against influenza infection. Respiratory Research. 2007 May 17;8(1):38.
91. Olive M, Moerman F, Fernandez-Cassi X, Altermatt F, Kohn T. Removal of Waterborne Viruses by Tetrahymena pyriformis Is Virus-Specific and Coincides with Changes in Protist Swimming Speed. Environ Sci Technol. 2022 Apr 5;56(7):4062–70.
92. Hartler J, Trötzmüller M, Chitraju C, Spener F, Köfeler HC, Thallinger GG. Lipid Data Analyzer: unattended identification and quantitation of lipids in LC-MS data. Bioinformatics. 2011 Feb 15;27(4):572–7.
93. Perez-Riverol Y, Bai J, Bandla C, García-Seisdedos D, Hewapathirana S, Kamatchinathan S, et al. The PRIDE database resources in 2022: a hub for mass spectrometry-based proteomics evidences. Nucleic Acids Res. 2021 Nov 1;50(D1):D543–52.